

Spectral functions of Sr_2IrO_4 : Theory versus experiment

B Lenz¹, C Martins² and S Biermann^{1,3}

¹ CPHT, Ecole Polytechnique, CNRS, Université Paris-Saclay, Route de Saclay, 91128 Palaiseau, France

² Laboratoire de Chimie et Physique Quantiques, UMR 5626, Université Paul Sabatier, 118 route de Narbonne, 31400 Toulouse, France

³ Collège de France, 11 Place Marcelin Berthelot, 75005 Paris, France

E-mail: silke.biermann@polytechnique.edu

Abstract. The spin-orbit Mott insulator Sr_2IrO_4 has attracted a lot of interest in recent years from theory and experiment due to its close connection to isostructural high-temperature copper oxide superconductors. Despite of not being superconducting its spectral features closely resemble those of the cuprates, including Fermi surface and pseudogap properties. In this article, we review and extend recent work in the theoretical description of the spectral function of pure and electron-doped Sr_2IrO_4 based on a cluster extension of dynamical mean-field theory ("oriented-cluster DMFT") and compare it to available angle-resolved photoemission data. Current theories provide surprisingly good agreement for pure and electron-doped Sr_2IrO_4 , both in the paramagnetic and antiferromagnetic phases. Most notably, one obtains simple explanations for the experimentally observed steep feature around the M point and the pseudo-gap-like spectral feature in electron-doped Sr_2IrO_4 .

Keywords: iridate, electronic structure, spectral function, spin-orbit coupling, dynamical mean field theory Submitted to: *J. Phys.: Condens. Matter*

1. Introduction

Electronic Coulomb correlations are well-established as one of the main players determining the excitations and response properties of 3d transition metal oxides or f-electron compounds. The relatively modest spatial extension of the orbitals forming the valence states in these materials leads to comparably large effective local Coulomb interactions. They are in particular large enough to compete with the kinetic energy even when several partially filled valence states are involved. It is well-known from studies of the multi-orbital Hubbard model that the critical interaction strength needed to localize the electrons and induce a Mott insulating state grows with the orbital degeneracy [1, 2], translating the enhanced kinetic energy in the multi-orbital context.

Multi-orbital physics is rather the generic situation in transition metal oxides [3] and even more so in f-electron compounds. Examples include t_{2g} -systems such as titanates [4] or vanadates [5], or Mn-, Fe- or Ni-based e_g -oxides [6]. A notable exception are high-temperature superconducting cuprates, where a single hole in an otherwise completely filled 3d-shell can be dominantly attributed to an orbital of $d_{x^2-y^2}$ character, corresponding – in the parent compounds – to a nominally half-filled configuration. Most of the exotic properties of cuprates are directly or indirectly attributed to this specific situation [7, 8, 9] ‡.

Iridium oxides have added interesting twists to these quite general considerations [12]. First, the rather extended nature of the Ir 5d orbitals would suggest correlations to play a minor role in these systems if indeed all three t_{2g} orbitals were contributing to the low-energy physics around the Fermi level in a more or less degenerate way. The effective local Coulomb interactions have rather modest values of the order of 2 eV [13, 14, 15], comparable to the t_{2g} -electron bandwidth, and would – in a degenerate three-orbital model – at most lead to a modest mass enhancement in a metallic state [13]. A radically different situation is realized in nature: focussing on the prototypical Sr_2IrO_4 , one is dealing with an insulating material with a strongly temperature-dependent gap, both in its low-temperature magnetic and high-temperature paramagnetic phase, as confirmed by x-ray photoelectron [16, 17, 18, 19, 20], angle-resolved photoemission [12, 21, 20, 22, 23, 24, 25, 26, 27, 28, 29, 30], and scanning tunneling [31, 32] spectroscopy, optical conductivity measurements [33, 34, 35, 36, 37, 38] as well as magneto [39, 40], thermo [41], and electrical [42, 43, 44, 45, 46] transport measurements.

From the theoretical point of view, Sr_2IrO_4 has been investigated by density functional theory in combination with single-site dynamical mean-field theory [13, 14, 47, 31, 22] or its cluster extensions [48, 30, 49], the self-consistent Born approximation [50] or the self-consistent Hartree-Fock method [51].

The system does not explore the full space of orbital fluctuations corresponding to the nominal t_{2g}^5 configuration, but rather adopts cuprate-like single orbital physics. The microscopic reason can be found in a subtle interplay between spin-orbit interactions,

‡ However, it should be noted that such a one-band minimal model has been repeatedly questioned to reproduce all eminent features of cuprate physics [10, 11].

structural distortions and Coulomb correlations [13, 15]. The former two result in a rearrangement of the electronic states in such a way that – at the one-particle level – two nearly filled bands (usually labeled by an effective quantum number $j_{\text{eff}} = 3/2$) and a half-filled ($j_{\text{eff}} = 1/2$) band can be identified. The role of the Coulomb correlations is then two-fold: first, to enhance the spin-orbital polarization of this state such as to leave only the now exactly half-filled $j_{\text{eff}} = 1/2$ at the Fermi level, and second, to localize the hole in this state.

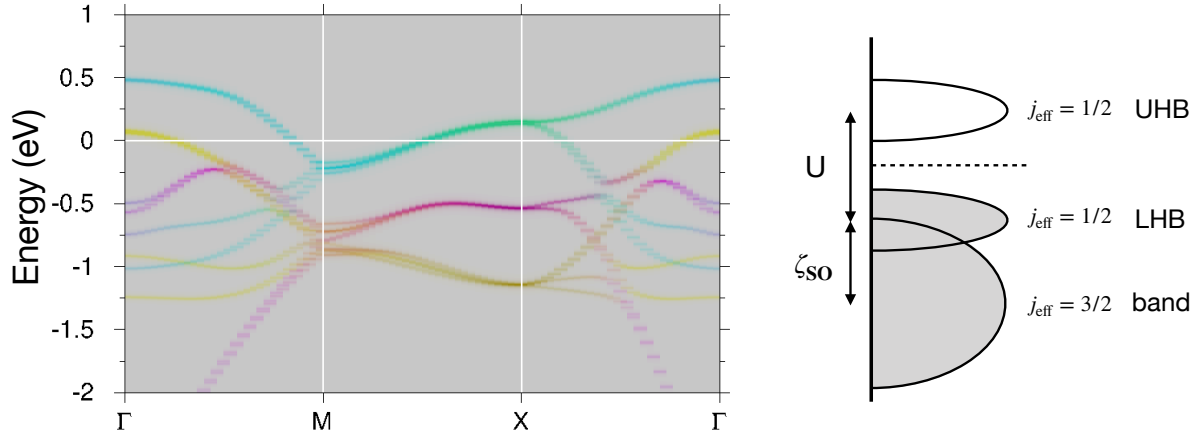


Figure 1. Left: Wannier-projected $j_{\text{eff}}=1/2$ (turquoise) and $j_{\text{eff}}=3/2$ bands ($|m_j| = 1/2$ in magenta, $|m_j| = 3/2$ in yellow) within DFT+SOC. Right: After applying Coulomb interactions, the $j_{\text{eff}}=1/2$ manifold splits into an upper and lower Hubbard band. Level scheme adopted from *Kim et al. 2008* [12].

The net result is thus an insulating state that bears some resemblance to the one of the parent compounds of the cuprates: it is realized within a layered crystal structure that deviates from the one of the celebrated La_2CuO_4 cuprate only by rotations of the oxygen octahedra around the crystallographic c -axis; it is of single-orbital nature, and it is accompanied by antiferromagnetic order in the low-temperature regime. It has been noted that Sr_2IrO_4 could be described by a twisted Hubbard model [52], bridging to the most popular model for high-temperature superconducting cuprates. In both cases, the antiferromagnetic order is driven by superexchange constants, which are of the same order of magnitude for Sr_2IrO_4 (nearest neighbor exchange J_{NN} between $\sim 0.06\text{eV}$ [53, 54] and $\sim 0.1\text{eV}$ [17]) and its related cuprate La_2CuO_4 ($J_{NN} \sim 0.14\text{eV}$ [55]). In Sr_2IrO_4 , a canted antiferromagnetic ground state is formed below the Néel temperature of $T_N \sim 240\text{K}$, which amounts to a weak ferromagnetic moment in c -direction [56].

Doping by chemical substitutions or vacancies leads in the cuprates to by now well-characterized but still intriguing superconducting phases. In iridates, doping has been achieved by La- [57, 42], Rh- [42], or Co-substitutions [58], O-vacancies [59] and surface-doping [20, 29]. From those, in particular Lanthanum and Rhodium substitutions have been used in recent years to systematically study electron- and hole-doped Sr_2IrO_4 respectively. In both cases, the substitutions primarily act like electronic doping and do not change much the lattice constant of Sr_2IrO_4 [42, 57]. Yet, any direct observation of

superconductivity remains elusive. In the cuprates, the normal state is itself anything but normal: the most intriguing feature is probably the appearance of a pseudogap in the low-energy electronic states in immediate vicinity to the Fermi level [60], which has continued to stimulate experimental [61, 62, 63, 64] and theoretical [65, 7, 8] studies.

Over the last decades, spectroscopic techniques have evolved into a most powerful tool to characterize low-energy excitations in correlated materials in a direct fashion (for a review, see e.g. [66]). Up to matrix elements translating modulations induced by light-matter coupling, angle-resolved photoemission measures the spectral function $A(k, \omega)$ related to the one-particle Green's function by

$$A(k, \omega) = -\frac{1}{\pi} \text{Tr} \text{Im} G(k, \omega). \quad (1)$$

The latter is in principle accessible by advanced many-body techniques, such as dynamical mean field theory (for reviews see [67, 68]) and its extensions. Recent advances using combined density functional theory dynamical mean field schemes [69, 70, 71] have made substantial progress in describing spectral properties of correlated materials in an *ab initio* (i.e. materials-specific) fashion (see e.g. [72, 73, 74, 75, 76, 77, 78]). Iridates have been in the focus since 2010 [79, 13, 14, 48, 47], with most recent advances giving a detailed account of spectral properties both in the pure and doped samples based on an extension of DMFT [30].

In this paper, we review and extend recent theoretical results using the cluster extension of DMFT proposed in Ref. [30] in comparison to available experimental data to assess the current state of the art in the field.

The paper is organized as follows: In the next section the oriented cluster dynamical mean-field theory of Ref. [30] is reviewed. Sections 3 and 4 focus on the paramagnetic high-temperature and antiferromagnetic low-temperature phase of undoped Sr_2IrO_4 respectively. We compare calculated spectra to experimentally measured ones in both cases. Electron-doped Sr_2IrO_4 is discussed in Sec. 5 with a focus on Fermi surface and pseudogap features of the spectral function. A summary and outlook conclude the paper in Sec.6.

2. Technique: Oriented Cluster Dynamical Mean-Field Theory

In dynamical mean-field theory (DMFT) [67, 68] the interacting many-electron problem is mapped onto a single impurity site that is coupled dynamically to a non-interacting bath. Since this impurity represents an arbitrary site in the lattice it amounts to a purely local description and correlation effects, which are taken into account via the impurity self-energy Σ_{imp} , are therefore local in nature, too. The momentum-dependent lattice Green's function is constructed using Σ_{imp} via

$$G(\mathbf{k}, \omega) = [\omega + \mu - H(\mathbf{k}) - \Sigma_{\text{imp}}(\omega)]^{-1}. \quad (2)$$

In the case of Sr_2IrO_4 , the one-particle hamiltonian $H(\mathbf{k})$ is obtained from a tight-binding fit of the $j_{\text{eff}}=1/2$ band, see Appendix A. The Green's function of the impurity

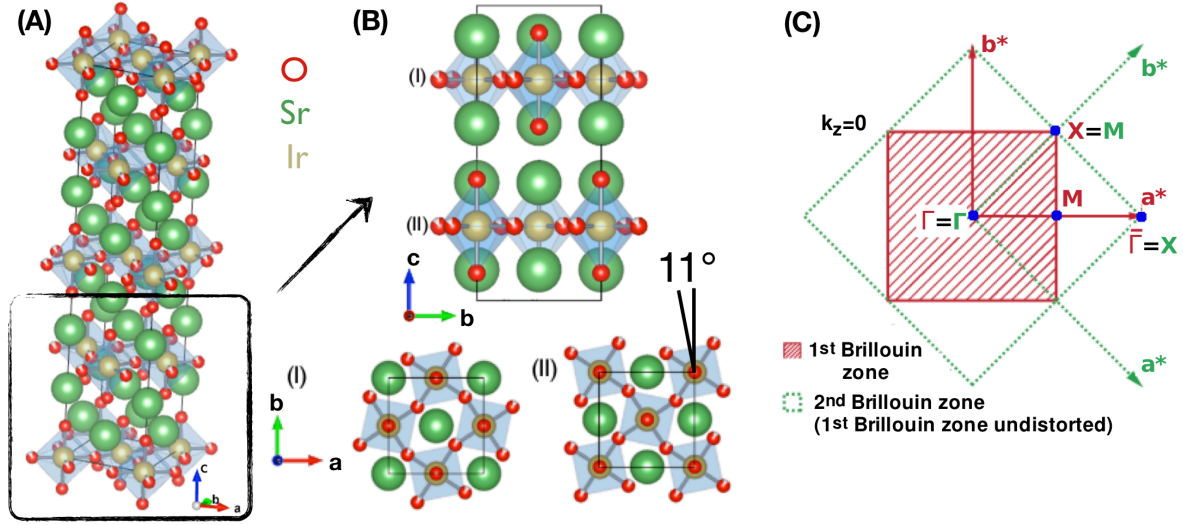


Figure 2. Crystal structure of Sr_2IrO_4 . Sr_2IrO_4 crystallizes in a $I4_1/acd$ structure (A) and can be described by a unit cell which comprises two Sr_2IrO_4 layers (I) and (II) in c -direction (B) with a total of four Ir atoms (two per layer). Within such a layer, the environments of neighboring Ir atoms differ since the surrounding oxygen octahedra are rotated by $\sim 11^\circ$ in opposite directions. Due to these rotations of the oxygen octahedra the unit cell is doubled and the respective Brillouin zone takes only half of the size of an undistorted geometry (C). Panels (B) and (C) adopted from *Martins et al.* [30].

problem is then equal to the local Green's function of the lattice problem, which is ensured by the DMFT self-consistency condition

$$G_{\text{loc}}(\omega) = \sum_{\mathbf{k}} G(\mathbf{k}, \omega), \quad (3)$$

which determines the bath and restores the translational invariance. In general, the system is of multi-orbital nature with multiple correlated shells a per unit cell. For each correlated site, the self-energy of the effective impurity site has to be rotated into the local reference frame via

$$\Sigma_a(\omega) = R_a^\dagger \Sigma_{\text{imp}}(\omega) R_a. \quad (4)$$

Here, Σ_{imp} is a matrix in orbital space, i.e. a $N \times N$ matrix for a system consisting of N correlated orbitals per correlated shell. If we assume that –due to crystallographic symmetries– the N_a correlated sites are equivalent, the overall self-energy matrix Σ is of size $N \cdot N_a \times N \cdot N_a$. Moreover, the self-energy is block-diagonal in the correlated shells, i.e.

$$\Sigma_{aa'}(\omega) = \delta_{aa'} \Sigma_a(\omega). \quad (5)$$

Since all shells are rotated into their local coordinate system, using the self-energy $\Sigma_{aa'}(\omega)$ in Eq.(2) leads to a lattice Green's function, which respects all point group symmetries of the crystal.

In cluster extensions of DMFT [80] the original lattice is tiled into (identical) clusters, which can break the point group symmetry of the crystal. The location \mathbf{x}

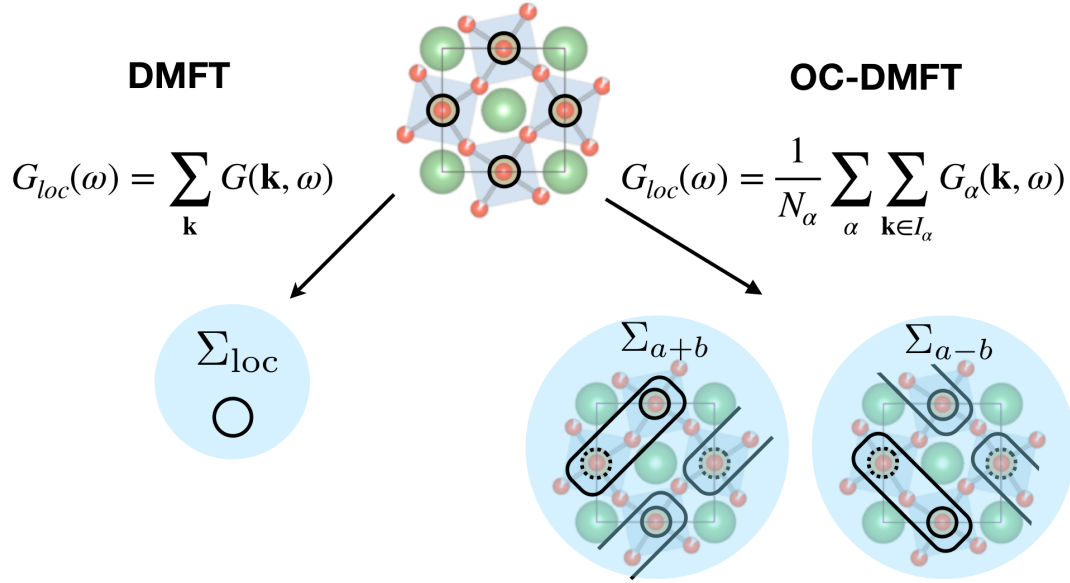


Figure 3. Comparison of DMFT and OC-DMFT: Since more than one cluster orientation is allowed, the self-consistency condition includes an orientation average which restores the point-group symmetry. In this case, the momenta \mathbf{k} have to be taken out of the Brillouin zone I_α corresponding to the respective orientation.

of each site can then be represented by specifying the origin of a cluster $\tilde{\mathbf{x}}$ and the site within the cluster \mathbf{X} . Using the self-consistency condition of Eq.(3) only restores the translational invariance, but does not remove possible violations of the point group symmetry. Instead of limiting ourselves to clusters, which have the full point group symmetry of the original lattice, we recently proposed to use oriented clusters and to restore the point group symmetry via a modified embedding condition [30]. Choosing an oriented two-atom dimer as a cluster, which represents two nearest-neighbor Ir sites, one is left with two possible (perpendicular) cluster orientations. Therefore, we can define a momentum-resolved Green's function evaluated with an orientation dependent self-energy:

$$G_\alpha(\mathbf{K}, \omega) = [\omega + \mu - H(\mathbf{K}) - \Sigma_{\text{dim}}^\alpha]^{-1}. \quad (6)$$

The momenta \mathbf{K} are taken out of the Brillouin zone corresponding to the Bravais lattice of the cluster locations $\tilde{\mathbf{x}}$ [80]. As a consequence, when constructing the local Green's function, the sum now runs over the two possible orientations $\alpha = x, y$ and over their corresponding momenta $\mathbf{K} \in I_\alpha$:

$$G_{loc}(\omega) = \frac{1}{N_\alpha} \sum_{\alpha} \sum_{\mathbf{K} \in I_\alpha} G_\alpha(\mathbf{K}, \omega). \quad (7)$$

The momentum-resolved spectral function $A(\mathbf{k}, \omega)$ to be compared with the ARPES spectra later on is obtained from the \mathbf{k} -resolved Green function

$$G(\mathbf{k}, \omega) = \frac{1}{N_\alpha} \sum_{\alpha} G_\alpha(\mathbf{k}, \omega). \quad (8)$$

Here, \mathbf{k} is the momentum-vector in the crystallographic Brillouin zone of the lattice.

For Sr_2IrO_4 neighboring Ir sites already differ in the rotation of their oxygen octahedra and the crystallographic unit cell consists of four Ir atoms. A possible choice for the unit cell amounts to taking two neighboring Ir sites in two stacked a-b layers in c-direction, see Fig. 2(A). Choosing two dimers as the building block for a cluster tiling of the lattice therefore does not change the Brillouin zone and keeps the same crystallographic cell.

Since we use the minimal cluster that incorporates non-local effects, it is possible to gain insight into the physical processes which cause certain features in the spectrum. For instance, inter-site fluctuations of the dimer are of antiferromagnetic spin nature and are encoded in the non-local part of the cluster self-energy. The latter can be seen as energy-dependent modulations of the inter-site hopping processes that enter in the Green's function G_α . In Sr_2IrO_4 this selection of an orientation α causes a $x - y$ -symmetry breaking in G_α . This shows the importance of the orientational average in Eq. (7), which restores this symmetry. Most interestingly, signatures of the fluctuations can be seen in terms of tilted lens-shaped Fermi surfaces in electron-doped Sr_2IrO_4 as discussed later in Sec. 5.

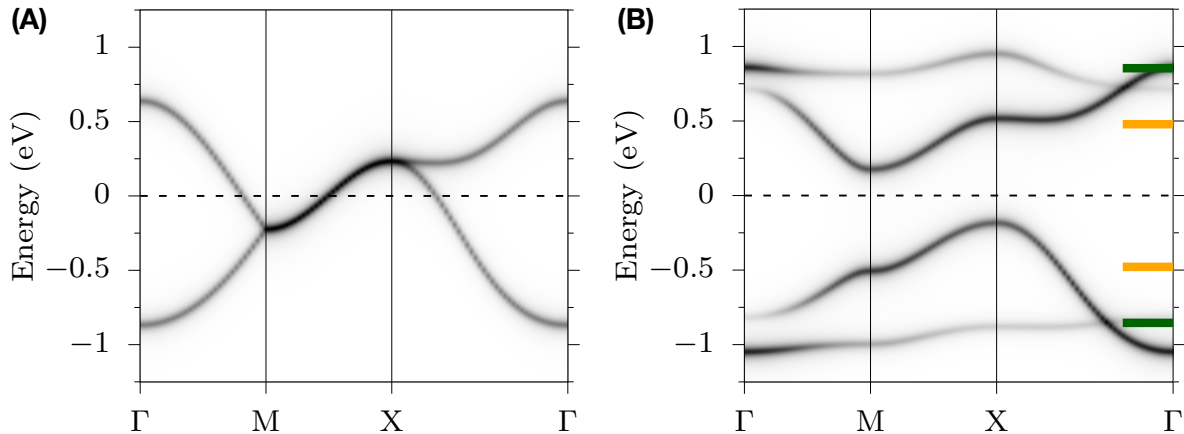


Figure 4. (A) The dispersion of one of the two downfolded inter-layer tight-binding bands constructed in Appendix A with chemical potential adjusted to match half-filling. (B) Effect of treating the Hubbard interaction $U = 1.1 \text{ eV}$ in Hubbard-I approximation via OC-DMFT. The four poles of the dimer Green's function are indicated by orange (green) lines and correspond to the bonding-/antibonding (satellite) bands.

Figure 4 illustrates schematically how including non-local fluctuations via the dimer self-energy Σ_α within OC-DMFT affects the spectral function. The starting point of the calculations is a tight-binding fit of the DFT $j_{\text{eff}}=1/2$ bands, which defines the bare dispersion $\epsilon(\mathbf{k})$. Since the unit cell comprises two layers in c-direction with a dimer each, we take the weak inter-layer hopping into account and obtain two slightly different downfolded inter-layer bands as discussed in Appendix A. For each of the two dispersions we then calculate the lattice Green's function for the two possible dimer orientations.

Choosing one dimer configuration changes the non-interacting spectrum of the band shown in Fig. 4(A) into the interacting spectral function $A_\alpha(\mathbf{k}, \omega)$ shown in (B). Besides the splitting of the band into a bonding and an antibonding band, additional satellite bands emerge at larger energy. For comparison, the bonding and antibonding poles of the dimer Green's function are indicated by orange, the position of their satellites by green lines.

We construct a Hamiltonian to model the $j_{\text{eff}}=1/2$ band which amounts to a one-band Hubbard model of interaction strength $U_{\text{eff}} = 1.1\text{eV}$ using a tight-binding modelling of the dispersion. This effective interaction U_{eff} takes into account the large nearest-neighbor interaction, which is due to the extended nature of the $5d$ orbitals. On the level of our dimer solver, the value of 1.1eV is in good agreement with recent constrained random phase approximation (cRPA) [81] estimates [13, 82]§ and produces a gap size of $\Delta \approx 0.3\text{eV}$ consistent with experiment [34]. Furthermore, if we assume strong coupling and do a rough estimation of the exchange coupling via $J = 4t^2/U_{\text{eff}}$, using the two different dispersions we obtain values of $J = 0.09\text{eV}$ and $J = 0.13\text{eV}$, which are close to the values determined from experiment [53, 54, 17].

To solve the cluster problem, we generalized to a two-site cluster the Hubbard-I solver [83]. Hubbard-I consists in neglecting the hybridization in the calculation of the self-energy and is therefore appropriate for materials in the strong-coupling limit. For this reason it has for example been used for rare-earth elements and materials [70, 84]. Here, our philosophy is different: We will show in the following that the dimer Hubbard-I approximation gives an excellent account of the spectral properties of Sr_2IrO_4 despite its proximity to the Mott transition. For more details on the technique itself, the cluster Hubbard-I solver used for the calculations and how to determine a thermodynamically consistent charge, we refer the reader to the supplementary material of Ref. [30] and references therein. Further details on the Hubbard dimer can be found in Ref. [85].

3. Sr_2IrO_4 in the Paramagnetic High-Temperature Phase

At high temperatures, Sr_2IrO_4 is a paramagnetic spin-orbit Mott insulator [12]. In the following section we discuss the spectral function in this paramagnetic phase, both calculated from OC-DMFT and measured using ARPES.

3.1. Spectra from Theory

Figure 5 shows the spectral function as well as their $j_{\text{eff}}=3/2$ and $j_{\text{eff}}=1/2$ parts along the path $\Gamma - M - X - \Gamma$. The model shows a gapped spectrum with the highest occupied states residing at the X point, while the lowest unoccupied states are at the M point.

In the $j_{\text{eff}}=1/2$ manifold, one can identify four separate peaks out of which the bonding and antibonding ones have largest spectral weight. Furthermore, one sees

§ For a dimer, the nearest-neighbor interaction V reduces the on-site interaction U to $U_{\text{eff}} = U - V$. After averaging the cRPA interaction values over the three t_{2g} orbitals, one arrives at values of $U_{\text{eff}} = 1.3\text{eV}$ [13] or $U_{\text{eff}} = 1.0\text{eV}$ [82].

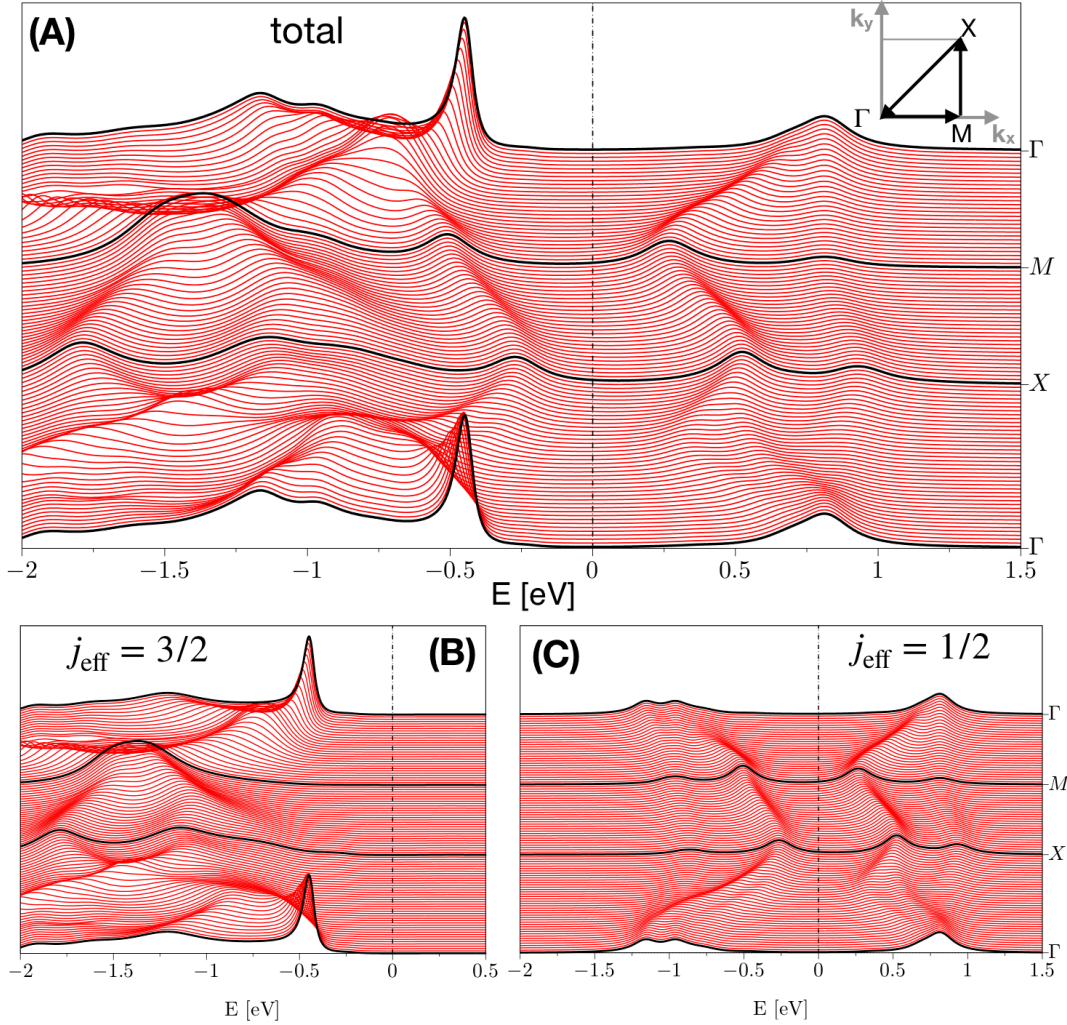


Figure 5. Calculated spectral function $A(\mathbf{k}, \omega)$ of pure Sr_2IrO_4 in the paramagnetic high-temperature phase along the \mathbf{k} -path $\Gamma - M - X - \Gamma$, which is shown in the inset of (A). The contribution of the filled $j_{\text{eff}}=3/2$ bands is shown in (B) and the spectral weight of the half-filled $j_{\text{eff}}=1/2$ band in (C).

small satellites in the electron- and hole-spectrum, as can be seen in Fig. 5(C). The bonding-antibonding splitting of two neighboring iridate layers in c -direction is much smaller such that it does not give rise to further splitting into separable peaks.

The $j_{\text{eff}}=3/2$ band does not cross the Fermi level and is completely filled. Still, it is responsible for spectral features at low energies such as the highest occupied states at and close to the Γ point. Away from the Γ point, the $j_{\text{eff}}=3/2$ manifold mainly contributes spectral weight at energies $E < -1\text{eV}$.

3.2. Experimental Spectra

In angle-resolved photoemission spectroscopy it is difficult to investigate insulators due to the build-up of surface charge. However, for insulators with a small gap like Sr_2IrO_4 it is feasible to measure the spectral function at moderate temperatures (in case of

Sr_2IrO_4 without further ado for synchrotron radiation down to $T \sim 50\text{K}$ [24, 23, 28]). Most of the photoemission studies on Sr_2IrO_4 focussed on the low-temperature phase, which shows antiferromagnetic long-range order of the $J = 1/2$ pseudospins. Up to our knowledge there is only one recent study presenting photoemission spectra in the paramagnetic high-temperature phase [30].

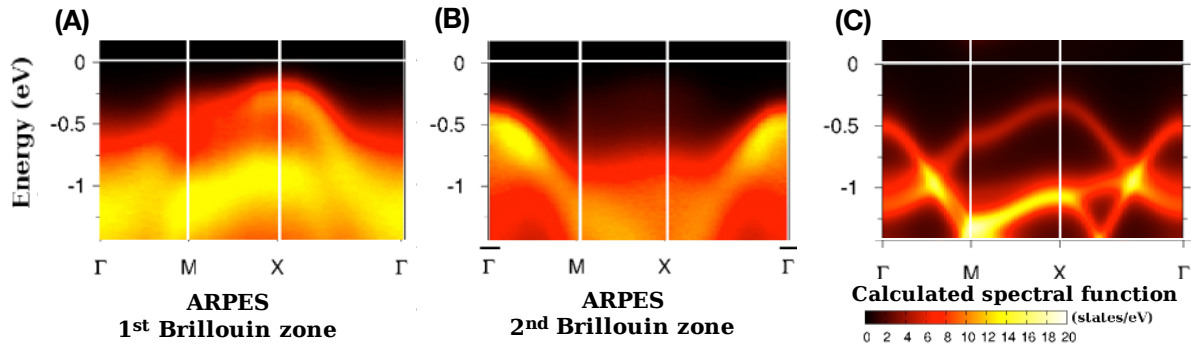


Figure 6. ARPES spectra at room temperature in the first (A) and second (B) Brillouin zone, as well as the calculated spectrum (C), adapted from Martins et al. 2018 [30]. Since the calculation does not include matrix-element effects, one should compare the weighted combination of spectra (A) and (B) with spectrum (C). Figure adapted from *Martins et al.* [30].

Figure 6(A) and (B) show the ARPES spectra taken at room temperature along the high-symmetry path $\Gamma - M - X - \Gamma$ for the first and second Brillouin zone, compare also with Fig. 2(B). Although the rather high temperature causes considerable thermal broadening, different bands can still be identified. In particular, the spectra in the first and second Brillouin zone differ drastically due to matrix element effects: In the first BZ spectral weight of the $j_{\text{eff}}=1/2$ band is enhanced whereas the second BZ is clearly dominated by contributions of the $j_{\text{eff}}=3/2$ manifold. Consequently, the first removal state at Γ , which is of $j_{\text{eff}}=3/2$ character, is found in the second BZ and the first removal state at X in the first BZ.

In Fig. 6(C) the calculated spectrum in the PM phase is shown along the same path in the first BZ. Due to the rotations of the oxygen octahedra the unit cell is doubled as compared to the undistorted structure (see, e.g., Ba_2IrO_4 [86]) and the bands are backfolded at the boundary of the (reduced) Brillouin zone. In the theory, by definition, there is no difference between first and second BZ. A quantitative comparison would require a calculation of the photoemission matrix elements which is beyond the scope of the present work. Nevertheless it is clear that a meaningful qualitative comparison can be obtained by assuming that features of the spectral function should show up in experiment either in the first or the second BZ.

Comparing with the calculated spectra, the spectral feature in the first BZ at the bonding energy $E_B \sim 1\text{eV}$ between M and X can be clearly attributed to be of $j_{\text{eff}}=3/2$ character. More precisely, the features of $j_{\text{eff}}=3/2$ character in the first BZ stems from the $m_j = 3/2$ band whereas the spectrum in the second BZ originates from the $m_j = 1/2$

band.

The stark differences between spectra in the first and second BZ indicate that the symmetry breaking potential which doubles the unit cell is rather weak: In case of strong symmetry breaking that reduces the symmetry from I_4/mmm to I_4/acd , the two Brillouin zones would show very similar spectra. Here, however, the distortions of the oxygen octahedra introduce only a small Fourier component of the corresponding potential. In addition, the polarization of the photons naturally leads to matrix element effects that enhance or suppress spectral weight in an orbital-selective manner [87, 88].

In contrast to single-site DMFT [30] or LDA+U+SOC [21] spectra, the present OC-DMFT spectrum correctly captures the absence of a weakly dispersive branch of $j_{\text{eff}}=1/2$ character at the Γ point with an onset at -0.2eV below the Fermi energy. As can be seen from figure 6(B) the onset of spectral weight at the Γ point is only at -0.5eV and should have rather $j_{\text{eff}}=3/2$ character showing a drastic difference to the spectrum calculated in DMFT. The reason of this improvement lies in the explicit inclusion of inter-site fluctuations: Antiferromagnetic short-range fluctuations within the dimer provide the previously missing ingredient. The energy scale of this inter-site fluctuations can be estimated as described in Ref. [30] as 108meV (78meV) for the interlayer (anti)bonding $j_{\text{eff}}=1/2$ states. This values compare well with an experimental estimate for the magnetic exchange coupling in the paramagnetic phase $J \sim 0.1\text{eV}$ obtained from the temperature dependence of the in-plane correlation length within resonant magnetic x-ray scattering [17].

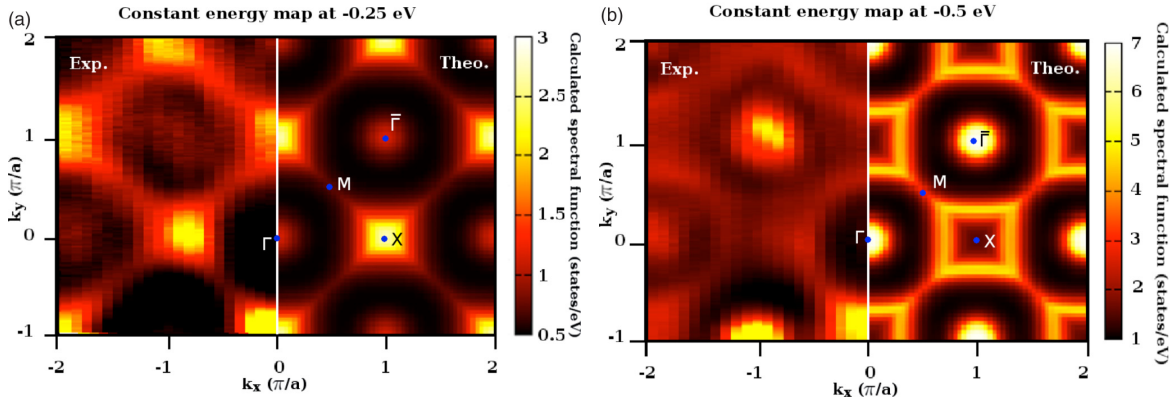


Figure 7. Constant energy maps at binding energies $E_B = 0.25\text{eV}$ and $E_B = 0.5\text{eV}$ measured in experiment (left) and calculated within OC-DMFT (right), adapted from *Martins et al.* 2018 [30]. The high-symmetry points of the Brillouin zone are indicated by blue points. The first and second Brillouin zone are the same in the calculation, but differ due to matrix-element effects in experiment.

To compare the ARPES spectra further with calculated spectral functions, figure 7 shows equal energy maps at $E_B = 0.25\text{eV}$ and $E_B = 0.5\text{eV}$. The constant energy maps are very similar to those taken below T_N in the antiferromagnetic phase [12, 21, 28], which shows that the photoemission spectra are not sensitive to long-range magnetic order. At $E = -0.25\text{eV}$, the peak at X due to the $j_{\text{eff}}=1/2$ band is well visible in both

experiment and theory, whereas the weak precursor at the Γ point is barely visible in the experiment and shows intensity modulations between different BZs. For $E = -0.5\text{eV}$, the intense blobs at Γ' and much weaker peaks at Γ show strong matrix element effects in the ARPES spectrum. Apart from these matrix element effects, both spectra are again in good agreement.

4. Sr_2IrO_4 in the Antiferromagnetic Low-Temperature Phase

So far we discussed the paramagnetic phase of pure Sr_2IrO_4 at temperatures above the Néel temperature of $T_N \sim 230\text{K}$ [12]. Below T_N the $j_{\text{eff}}=1/2$ pseudospins of Sr_2IrO_4 order and a phase transition towards an antiferromagnetic phase occurs [43]. Since the moments are slightly tilted out of plane, the ground state is rather a canted antiferromagnet [56, 89]. In this section we will discuss the spectral properties of the antiferromagnetically ordered low-temperature phase of Sr_2IrO_4 .

4.1. Spectra from Theory

Starting from the same effective one-band Hubbard model, but allowing for antiferromagnetic ordering within the dimers of the different planes leads in the OC-DMFT treatment to an AF ground state at low temperatures. In our cluster treatment we assume an antiferromagnetic alignment of the $j_{\text{eff}} = 1/2$ moments on neighboring Ir spins. This is done by including an antiferromagnetic Weiss field on the cluster, whose strength is determined via a variational principle using self-energy functional theory [90, 91]. One should note that the experimentally measured magnetic configuration shows additional spin canting and leads to an effective weak ferromagnetic moment [56]. From a modeling point of view this can be included via a twisted Hubbard model [52]. Since we focus here rather on spectral than on magnetic properties we keep an antiferromagnetic alignment of the moments, which -in principle- slightly overestimates the magnetization. The corresponding spectral function for pure Sr_2IrO_4 in this AF configuration is shown in figure 8.

The antiferromagnetic spectrum is very similar to a paramagnetic spectrum calculated for the same temperature. This similarity is due to antiferromagnetic fluctuations, which are the essential ingredient for a precise description of the spectral function of paramagnetic Sr_2IrO_4 . Compared to the paramagnetic spectrum, the splitting between (anti)bonding band and (upper) lower Hubbard satellite band is a bit enhanced. As a consequence, the two different contributions to the hole part of the spectrum at Γ can now be identified, whereas the paramagnetic spectrum of Fig. 5(C) shows only one single peak at $\sim 0.6\text{eV}$. Furthermore, some spectral weight is transferred from the (anti)bonding bands to the satellites. Although it is only a minor change, the antiferromagnetic ordering leads thereby to additional spectral weight between X and M at $\sim -1\text{eV}$.

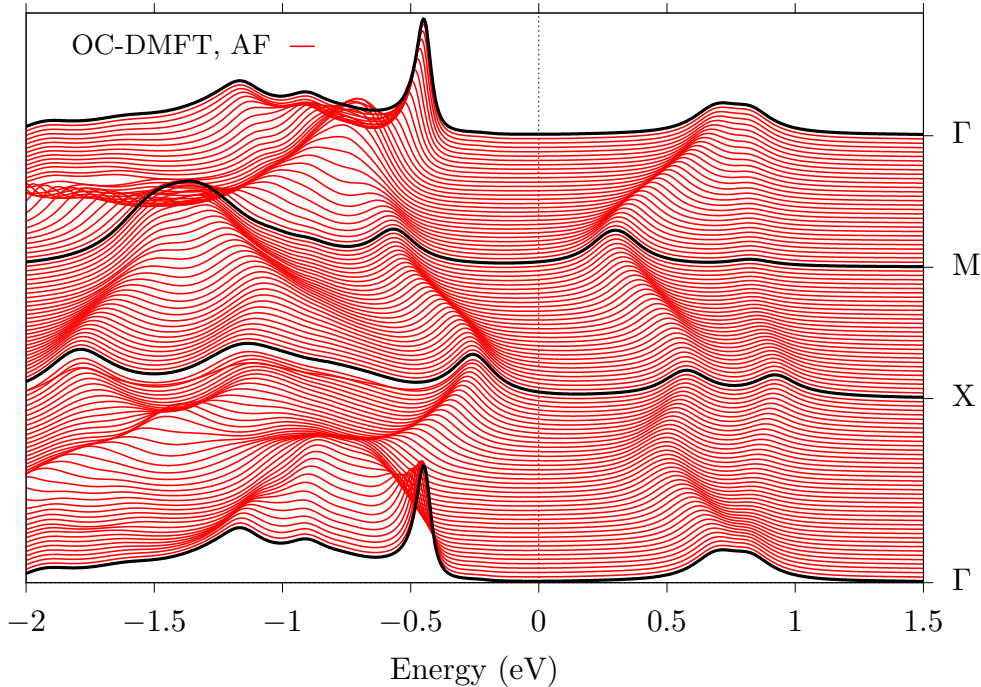


Figure 8. Calculated spectral function $A(\mathbf{k}, \omega)$ along the \mathbf{k} -path $\Gamma - M - X - \Gamma$ in the antiferromagnetic low-temperature phase.

4.2. Experimental Spectra

Using angle-resolved photoemission spectroscopy to investigate pure Sr_2IrO_4 is limited to moderate temperatures due to surface charging effects that prevent an investigation of the sample at very small temperatures. Nevertheless, spectra for temperatures down to $T = 20\text{K}$ have been measured [25], which is deep in the antiferromagnetic phase. Although the data quality is not as high as for doped samples, which are metallic and do not have this problem, the spectra allow for the extraction of dispersion that can be compared to our calculated spectrum, see Fig. 9. Overall, the calculated spectrum is in good agreement with the different experimental data sets. Since the experimental data shown were taken under different experimental conditions like temperature, photon energy or polarization, the dispersions vary a bit. This is in particular visible at the upper band edge close to the X point, where the position of the $j_{\text{eff}}=1/2$ band maximum varies by several 100meV between the different works.

In order to compare the spectra more quantitatively, we plot the calculated spectral function at the high-symmetry points Γ , M , and X with the energy distribution curves (EDC) of different experimental studies in figure 10. Again, the calculated spectral function reproduces all features of the experimental EDCs at least qualitatively. Modulations at larger bonding energies $E \leq -1\text{eV}$ are more pronounced in the calculated spectra than in experiment, but the low-energy region compares favorably. At Γ and X the onset of spectral weight and the position of maximal intensity agrees well between calculation and experiment. However, at M the peak position in the

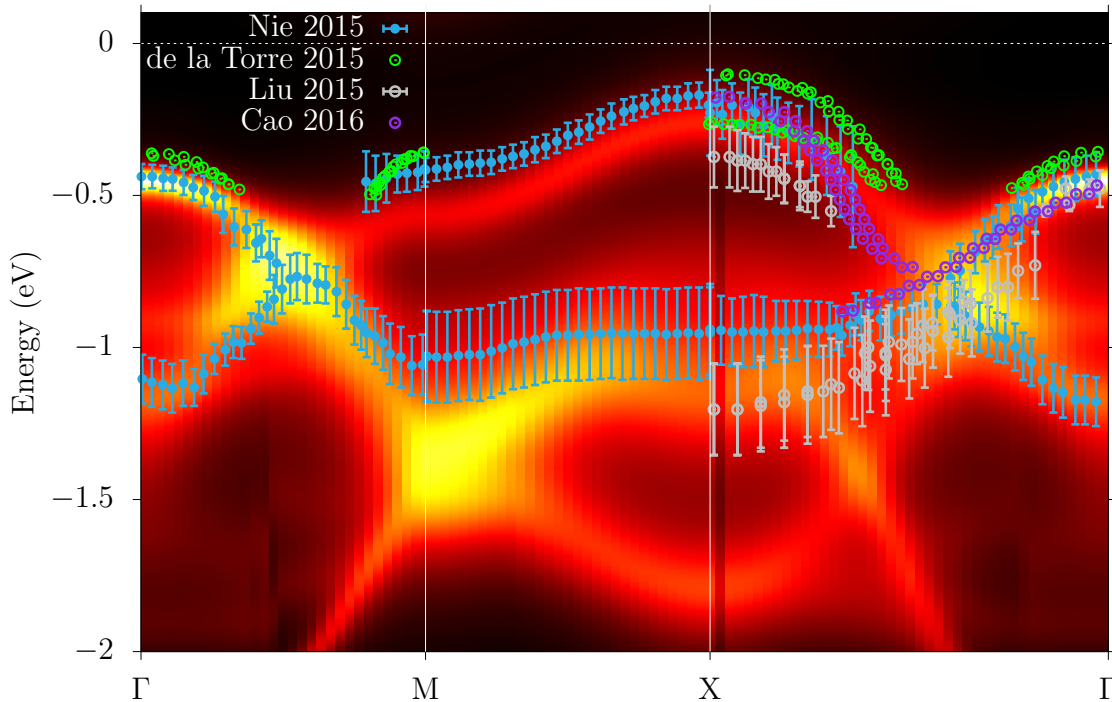


Figure 9. Comparison of the calculated spectral function $A(\mathbf{k}, \omega)$ with dispersions extracted in ARPES works. Experimental data shown is extracted from *Nie et al. 2015* [26], *de la Torre et al. 2015* [24], *Liu et al. 2015* [25], and *Cao et al. 2016* [28].

calculated spectrum is at smaller energy than in experiment. One might think of two reasons for this deviation. First, it is known that antiferromagnetism is overestimated within a dimer cluster and therefore leads here to a stronger splitting between bonding and antibonding band. Secondly, the ground state of Sr_2IrO_4 at low temperatures is a canted antiferromagnet whereas on the cluster level the system adopts a purely antiferromagnetic configuration with larger net staggered magnetization.

Quite generally one observes that the spectra in PM and AF phases are very similar ||. This is consistent with our finding that our dimer approach, which introduces AF fluctuations, provides an extremely good description of the PM. It also explains the success of AF DMFT calculations even in its single-site version to describe both phases. Note that an AF ordered dimer is well described by a mean-field description and the AF ordered insulator can -in this sense- be considered a band insulator. This effect explains the apparent success of DFT+U-like descriptions of spectra of Sr_2IrO_4 [12, 47], which however strongly differ from experiment at the Γ and M point.

|| Interestingly, a similar trend has also been found in the undoped cuprate $\text{Sr}_2\text{CuO}_2\text{Cl}_2$, where ARPES spectra in PM and AF phases are much akin [93].

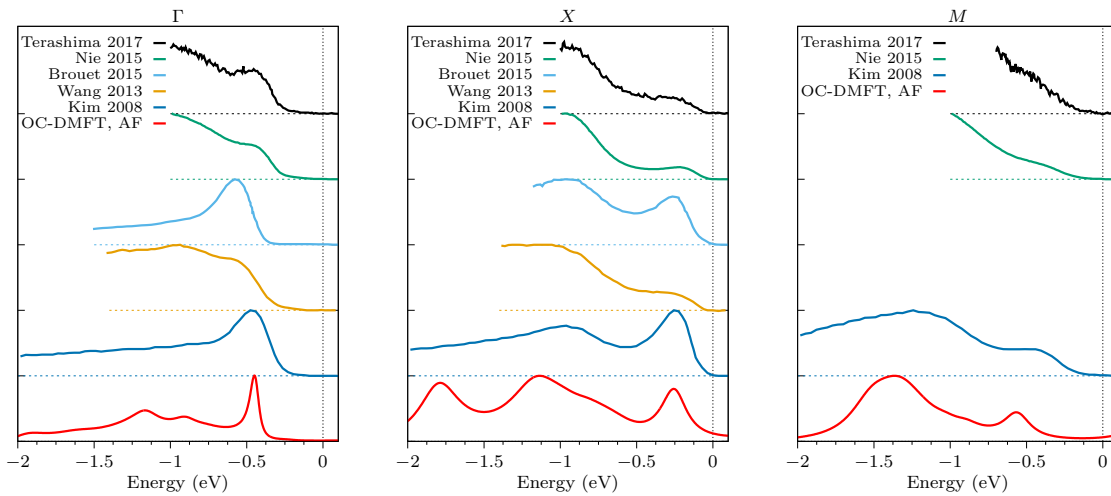


Figure 10. Detailed comparison of the calculated spectral function (red) and different ARPES measurements at the high-symmetry \mathbf{k} -points Γ , X , and M . The spectral weight curves have been normalized with respect to the available maximal weight of the respective curves and dashed lines indicate the zero-intensity offsets of the respective curves. Some key properties of the experimental measuring conditions used in these works can be found in table B1. Experimental data are extracted from *Kim et al. 2008* [12], *Wang et al. 2013* [21], *Brouet et al. 2015* [23], *Nie et al. 2015* [26], and *Terashima et al. 2017* [92].

4.3. Constant Energy Cuts

In figure 11 we compare the calculated constant energy maps of Sr_2IrO_4 in the antiferromagnetic phase at two different binding energies with ARPES spectra from Ref. [25]. Qualitatively, the features are well captured by the OC-DMFT calculation: At $E = -200\text{meV}$ only the $j_{\text{eff}}=1/2$ bands at the X points have non-zero spectral weight and theory and experiment only differ in the $x - y$ anisotropy of spectral intensity in experiment, which stems from matrix-element effects that are not taken into account in the calculation. Due to linear polarization of the photon beam in k_y direction the experimental spectra have larger spectral weight around X -points in k_y - than in k_x -direction, whereas the calculated spectra still show $x - y$ symmetry. Compared to Fig. 11A, at a binding energy of $E = 400\text{meV}$ both experiment and theory show in addition some spectral weight at the Γ point due to the $j_{\text{eff}}=3/2$ band, which is peaked at slightly larger binding energies. The main contribution of spectral weight still stems from the $j_{\text{eff}}=1/2$ band, however, in contrast to the measurement the calculated spectrum is not peaked at the X points, but rather around them. Good agreement with the $j_{\text{eff}}=1/2$ part of the measured spectrum would rather be obtained by assuming that the $j_{\text{eff}}=1/2$ part of the experimental spectrum corresponds in fact to slightly smaller binding energies than indicated. This can be seen in the third column of Fig. 11, where the $j_{\text{eff}}=1/2$ part of the calculated spectrum is in addition shifted by -0.15eV .

This is consistent with the comparison to other ARPES works shown in Fig. 9, where one sees that the dispersion of Ref. [25] is located at the X point at $\sim 0.1\text{eV}$

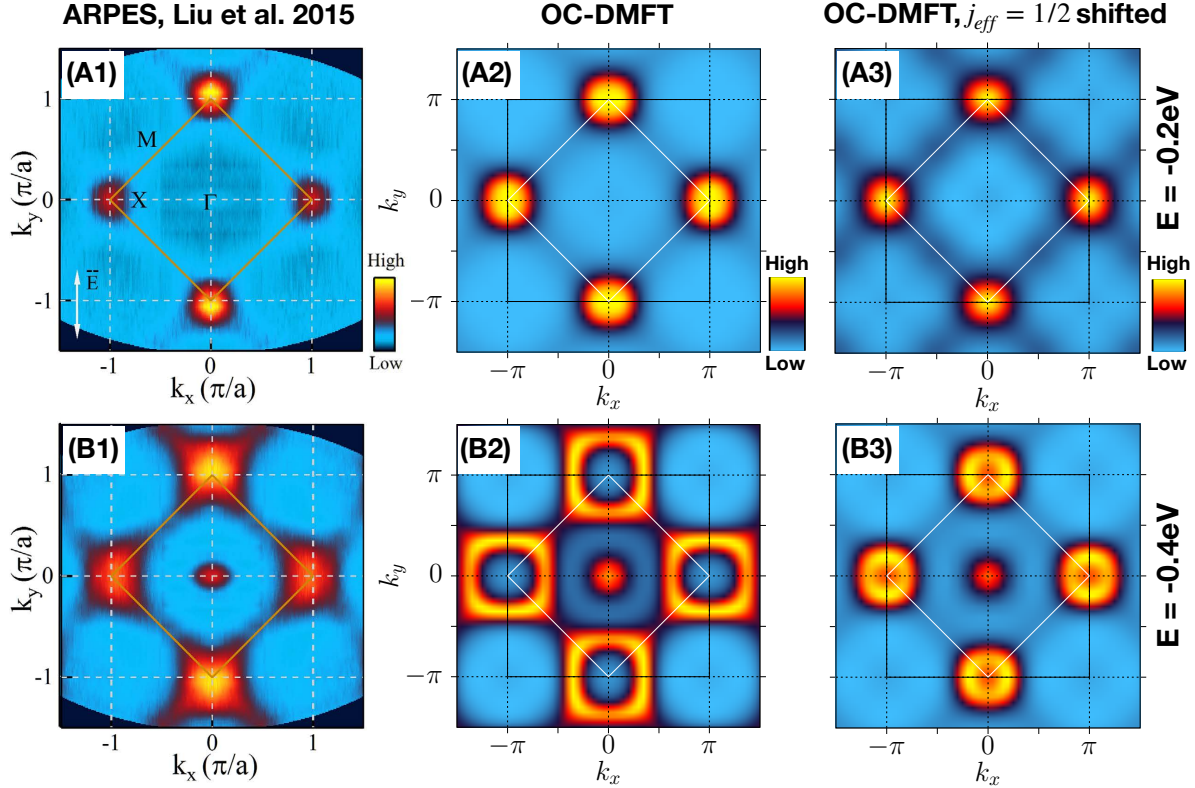


Figure 11. Constant energy maps of Sr_2IrO_4 in the antiferromagnetic phase at energies $E = -0.2\text{eV}$ (A) and $E = -0.4\text{eV}$ (B). The angle-resolved photoemission spectra at $T \sim 20\text{K}$ (A1,B1) are adapted from *Liu et al.* 2015 [25] and are compared to OC-DMFT spectra (A2,B2) at the same binding energies. (A3,B3) show the calculated spectra with an additional shift of -0.15eV for the $j_{\text{eff}}=1/2$ manifold, see text.

larger binding energies. We note that the dispersion at the Γ point is not affected, but rather consistent between the different ARPES data shown in Fig. 9. Therefore, the origin of the apparent slight difference of the energetic difference between $j_{\text{eff}}=1/2$ and $j_{\text{eff}}=3/2$ bands in the spectra of *Liu et al.* as compared to theory remains a puzzle.

5. Electron-doped Sr_2IrO_4 at Low Temperatures

The similarity of its electronic structure with hole-doped high-temperature cuprate superconductors has sparked interest in electron-doped Sr_2IrO_4 and triggered experimental and theoretical investigations in recent years. In contrast to the cuprates, no superconductivity has been found in Sr_2IrO_4 , it rather becomes a paramagnetic metal down to lowest temperatures for sufficiently strong doping. Nevertheless, spectral properties like pseudogap features inherent to cuprates have also been proposed for doped Sr_2IrO_4 [52, 24]. In this section, we will discuss the spectra of electron-doped Sr_2IrO_4 at low temperatures calculated from theory and compare it to ARPES measurements of La-doped samples.

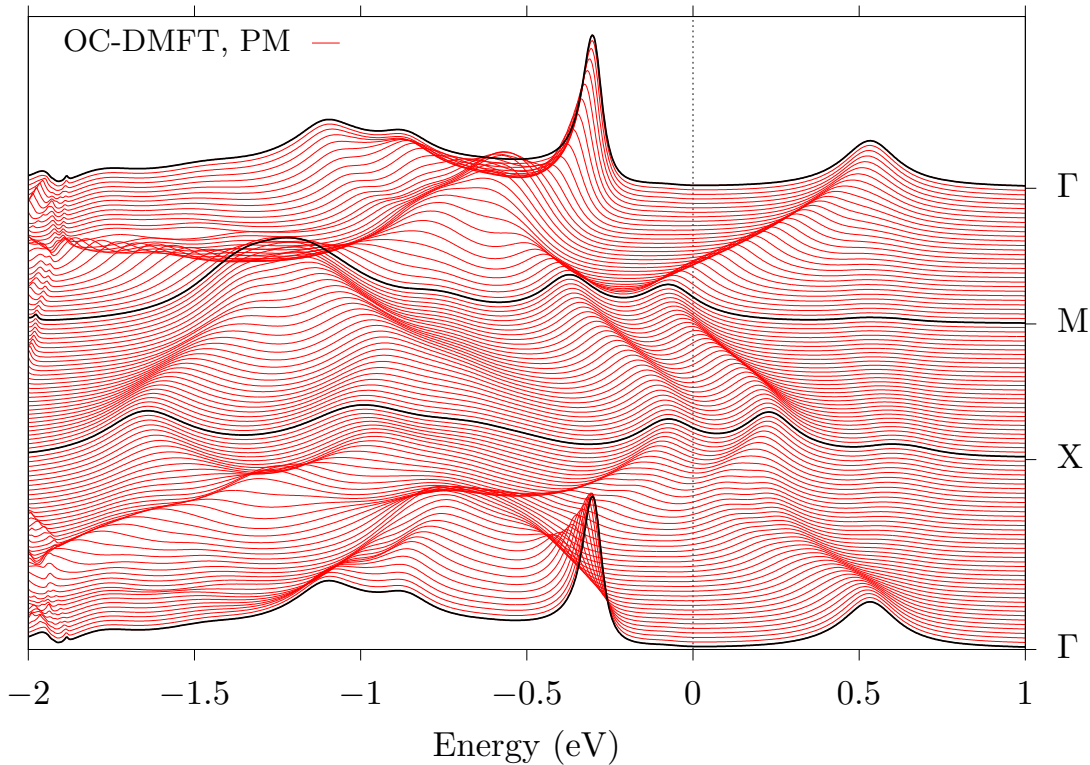


Figure 12. Spectral function $A(\mathbf{k}, \omega)$ of 10% electron-doped Sr_2IrO_4 along the \mathbf{k} -path $\Gamma - M - X - \Gamma$. Within this paramagnetic calculation we used an effective Coulomb interaction strength of $U = 0.6\text{eV}$.

5.1. Theoretical Spectra

In order to calculate the spectral function of electron-doped Sr_2IrO_4 we apply OC-DMFT to the $j_{\text{eff}}=1/2$ band at an electron filling of $n = 0.9$. It should be noted that the $j_{\text{eff}}=3/2$ bands are still completely filled and therefore not much affected by the change in the electron filling n , see Fig. 12.

For the $j_{\text{eff}}=1/2$ band the change in electron filling renders the system metallic. In a metal, electronic screening is much enhanced as compared to an insulator and as a consequence, the effective local Coulomb interaction strength is reduced [94]. Here, we take the enhanced screening into account by using an effectively reduced Coulomb interaction strength of $U_{\text{eff}} = 0.6\text{eV}$, which leads to good agreement of the calculated spectra with ARPES data. The corresponding spectral function $A(\mathbf{k}, \omega)$ is plotted in Fig. 12. Due to the electron doping, the Fermi surface now has pockets around the M point and the lower $j_{\text{eff}}=1/2$ branch is close to E_F at M. Note that we have not recalculated the position of the $j_{\text{eff}}=3/2$ states in the doped case from DMFT. Instead, we estimate an electrostatic shift of $\Delta E_{\text{Hartree}} = U\Delta n$, which was applied to the bands calculated in the undoped case.

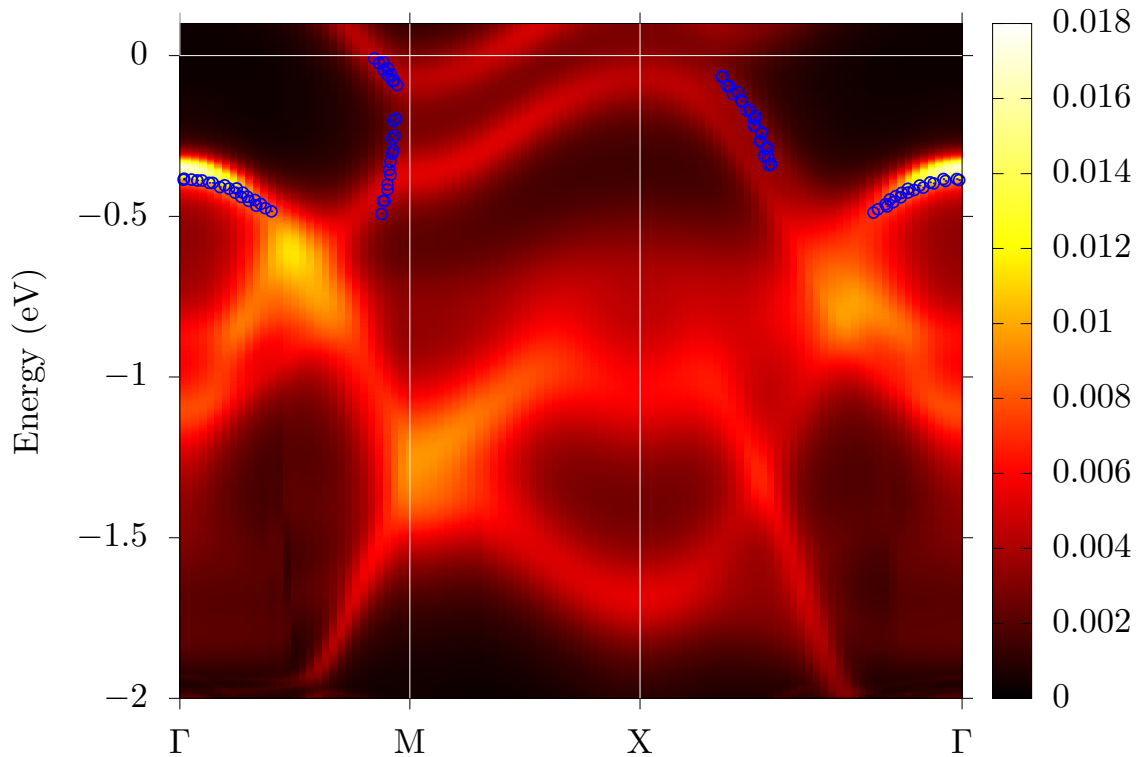


Figure 13. Comparison of the calculated spectral function of 10% electron-doped Sr_2IrO_4 with ARPES data of a $x = 0.05$ La-doped sample $(\text{Sr}_{1-x}\text{La}_x)_2\text{IrO}_4$. Experimental data points (blue) are extracted from *de la Torre et al.* [24].

5.2. Experimental Spectra

Most experimental works on electron-doped Sr_2IrO_4 focus on the low-energy region at and close to the Fermi level E_F . Before discussing two spectral features close to E_F in more detail in the following two subsections, we compare in Fig. 13 the calculated spectrum to available ARPES data of La-doped samples $(\text{Sr}_{1-x}\text{La}_x)_2\text{IrO}_4$.[¶]

The spectral feature of $j_{\text{eff}}=3/2$ character at the Γ point is correctly captured, as well as the dispersion of the upper $j_{\text{eff}}=1/2$ branch around the M point, which leads to pocket structures in the Fermi surface. Along the $\Gamma-X$ direction the $j_{\text{eff}}=1/2$ dispersion is captured with small deviations from the ARPES data of Ref. [24]. However, the calculated spectrum of the lower $j_{\text{eff}}=1/2$ branch deviates close to M from the measured photoemission spectrum and is discussed in the next subsection.

5.3. Spectra close to the M point

In this subsection, we focus on spectral properties around the M point, see Fig. 14.

In Ref. [24] *de la Torre et al.* suggested that the bands with nearly linear dispersion close to the M point might extrapolate to a Dirac point at $E \sim -0.1\text{eV}$ before they

[¶] Note that $x = 0.05$ thereby amounts to 10% electron doping.

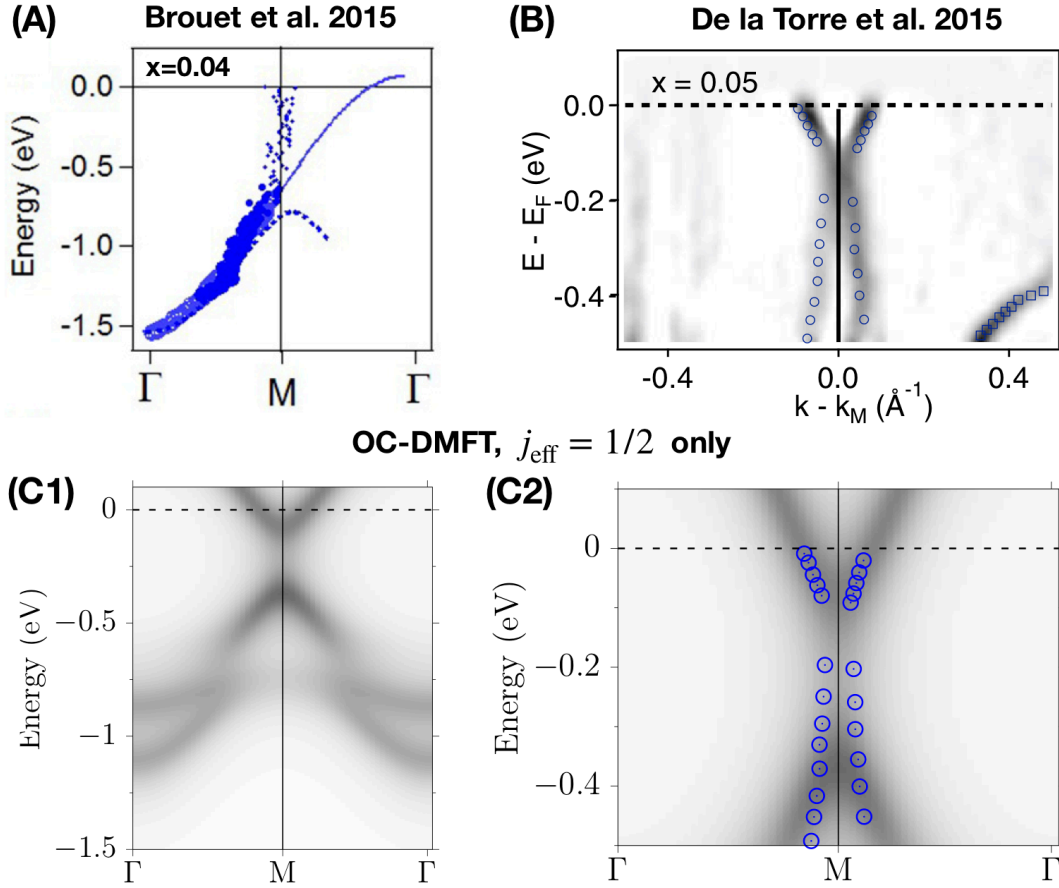


Figure 14. Comparison of ARPES spectra (A,B) with calculated spectra (C1,C2) around the M -point. (A) The dispersion extracted by MDC analysis along Γ - M for a sample with $x = 0.04$ La-doping, adopted from *Brouet et al.* [23]. The dots represent peak positions extracted from Lorentzian fits and follow the solid blue line up to -0.6eV . Close to the M point the correlation gap is indicated by the dashed blue line. (B) Curvature plots of ARPES raw data for a $x = 0.05$ doped sample, adapted from *de la Torre et al.* [24]. Blue dots indicate peak positions determined from this plot. (C1,2) show the calculated $j_{\text{eff}}=1/2$ spectra for 10% electron doped Sr_2IrO_4 in the two energy ranges of (A) and (B).

continue still with a quasi-linear dispersion up to the Fermi energy (Fig. 14(B)). For a slightly less La-doped sample, *Brouet et al.* found a very similar quasi-linear feature close to the M point [23], which is much reduced in intensity, but non-negligible. However, they interpret this feature as an artifact of the fitting procedure applied to the momentum distribution curves (MDC): Since the $j_{\text{eff}}=1/2$ energy distribution curve has a quite broad peak at lower energy the tail of this peak can lead to a signal with quasi vertical dispersion that is picked up in the MDC analysis. For the case of larger La-doping, where the states close to E_F clearly form a pocket around M , this suggests also a different interpretation of the signal for binding energies $E_B > 0.1\text{eV}$. Instead of a Dirac point of two connected bands, the region below $E \sim -0.1\text{eV}$ could be gapped and the spectral weight just be picked up by the broad tail of the lower $j_{\text{eff}}=1/2$ band

at lower energy.

To investigate this question we plot the $j_{\text{eff}}=1/2$ part of the calculated spectral function for 10% electron doping in Fig. 14(C1,2) once in a large energy region and once in close vicinity of the Fermi energy. As can be seen from (C1) the OC-DMFT spectrum is gapped in the region $-0.35\text{eV} \leq E \leq -0.1\text{eV}$ and has large spectral weight at M and $E \sim -0.4\text{eV}$. Along roughly half the distance $M - \Gamma$ the spectral features are in good agreement with (A), close to Γ spectral contributions from $j_{\text{eff}}=3/2$ render the comparison more difficult, but main features are qualitatively still comparable to (A). When comparing to (B) one notices good agreement for the band forming the pocket in the immediate vicinity of the Fermi energy. Also for energies $E \leq -0.35\text{eV}$ the spectrum agrees well with (B) suggesting a reinterpretation of the "gapped" region $-0.35\text{eV} \leq E \leq -0.1\text{eV}$ in terms of Ref. [23].

5.4. Fermi Surface, Electron Pockets and Pseudogap

For La-doping $x \geq 0.05$ the system is a paramagnetic metal with a Fermi surface with well-defined electron pockets. In Fig. 15 we compare ARPES spectra at the Fermi energy of 5% La-doped Sr_2IrO_4 with the calculated Fermi surface at 10% electron doping. The

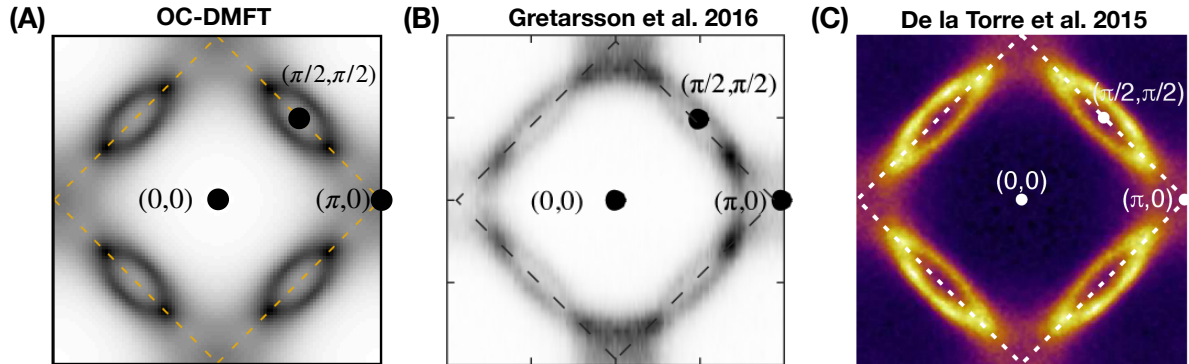


Figure 15. Fermi surface of 5% La-doped Sr_2IrO_4 within ARPES showing the Fermi pockets at $T = 10\text{K}$ (B), adopted from *Gretarsson et al.* [53], and at $T = 8\text{K}$ (C), adopted from *de la Torre et al.* [24]. The calculated Fermi surface at 10% electron-doped Sr_2IrO_4 is shown in (A).

electron pockets around the M points are lens-shaped with their elongated axis pointing towards the X points. Comparing position, shape and size of the pockets in (A) with the experimental observations leads to overall good agreement. Most spectral weight of the pockets is found at their tips, consistent with experiment ((B) and (C)). By symmetry, both sides of the pockets carry equal spectral weight in the theoretical spectral function. In the ARPES spectra, the spectral weight in the second BZ is enhanced as compared to the backfolded part of the pocket.

In experiments, resistivity measurements of La-doped samples display unusual metallic behavior at low temperatures [23, 24] and for $x = 0.05$ doped samples an anti-nodal pseudogap was found using ARPES [24], shown in Fig. 16(B). Since in

ARPES the hole-part of the spectrum cannot be accessed, one often uses the particle-hole symmetrized spectral function to extract pseudogap features. To compare with experimental findings, we plot this symmetrised spectral function in Fig. 16. Along the remnant Fermi surface, which in this case is a nearly circular path in \mathbf{k} -space, one then extracts the "gap" $\Delta(\alpha)$ of the symmetrised spectral function as a function of angle α . This gap is defined by the peak position ω^* of this spectral function closest to the Fermi level at a given \mathbf{k} -point, $\Delta(\alpha) = 2\omega^*(\mathbf{k}_\alpha)$.

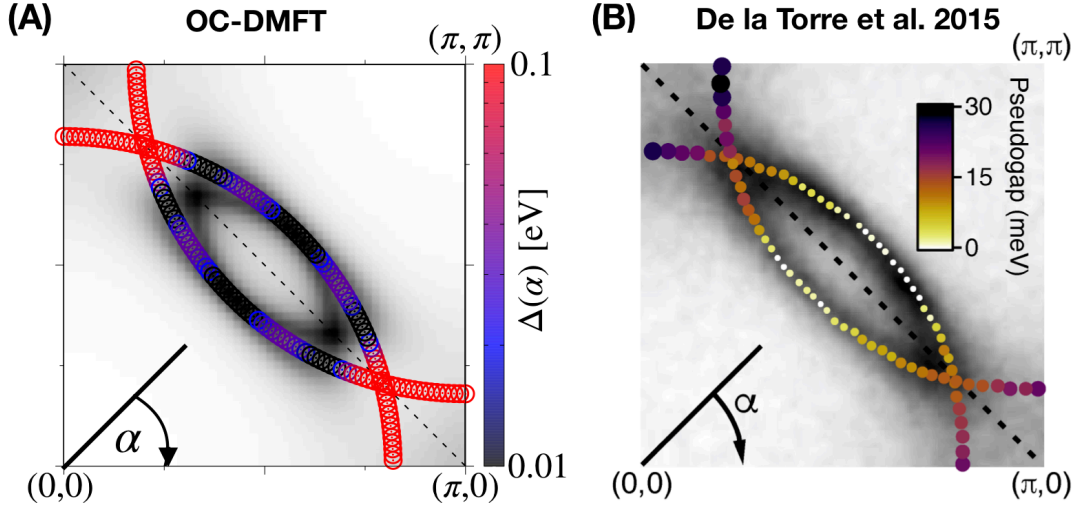


Figure 16. Calculated $\Delta(\alpha)$ of 10% electron-doped Sr_2IrO_4 (A) and measured pseudogap (B) of a 5% La-doped sample at $T = 8\text{K}$. In both cases, the quantities were extracted along the remnant Fermi surface as discussed in the text. Panel (b) is adopted from *de la Torre et al.* [24], BF denotes back-folded.

Comparing the calculated $\Delta(\alpha)$ in Fig. 16A with the pseudogap (PG) extracted in Ref. [24] from ARPES measurements (Fig. 16B) shows qualitatively similar features. Both $\Delta(\alpha)$ and the PG emerge at the tips and outside of the elliptical pocket along the circular \mathbf{k} -path. In addition, within the calculations even the pocket structure itself at small angles α shows regions of non-zero $\Delta(\omega)$. These spectral features can be tracked back to the average over the two perpendicular cluster orientations used within the OC-DMFT calculation [30]. To observe them separately would, however, require a very high resolution in experiment. Furthermore, the origin of the large $\Delta(\omega)$ values close to the antinodal point can be identified in the calculation by comparing to the full spectral function including the hole part. In contrast to the pseudo-gap-like features close to the tips of the pockets, the antinodal point shows a true gap since the spectral peaks closest to the Fermi energy belong to the $j_{\text{eff}}=3/2$ band.

6. Conclusion and Outlook

In this work we gave an overview of cluster-DMFT-based calculations of spectral functions of pure and electron-doped Sr_2IrO_4 . For undoped Sr_2IrO_4 we obtained good

agreement with ARPES spectra both in the antiferromagnetic and paramagnetic phase, and in the electron-doped system pocket structures of the Fermi surface and prominent pseudogap features of the spectrum could be reproduced.

As most theoretical works on Sr_2IrO_4 , also our work here is based on effective one-orbital descriptions of the correlated $j_{\text{eff}}=1/2$ bands and lead to good agreement with experiment. However, both *ab initio* calculations [79] and angle-resolved photoemission spectra [88, 87] revealed a strong \mathbf{k} -dependence of the t_{2g} contributions that form the effective $j_{\text{eff}}=1/2$ band. One of the challenges to future studies is to extend the current description to polarization-dependent ARPES spectra, where effects not captured in a local $j_{\text{eff}}=1/2$ picture could enter into play.

Furthermore, a question that has been raised recently is whether hidden orders such as the time-reversal symmetry breaking hidden order found in neutron scattering experiments [95] or the (different) hidden order investigated in Ref. [44] might influence spectral properties.

Acknowledgments

This work was supported by a Consolidator Grant of the European Research Council (Project CorrelMat-617196), the French Agence Nationale de la Recherche under project SOCRATE (Project No. ANR-15-CE30-0009-01) and supercomputing time at IDRIS/GENCI Orsay (Project No. t2018091393). We acknowledge helpful discussions with Steffen Backes, Fabrice Bert, Dalila Bounoua, Philippe Bourges, Veronique Brouet, Jaehong Jeong, Alex Louat, Luca Perfetti, and Yvan Sidis and we are grateful to the CPHT computer support team.

Appendix A. Tight-binding model

To capture the physics of the DFT bands of Sr_2IrO_4 , usual tight-binding models [96, 97, 49] describe the t_{2g} bands and then add spin-orbit coupling. In this work, we realized directly a tight-binding model for the j_{eff} bands to describe the DFT band structure, based on our understanding from the Wannier-projected characters (see Fig. 1).

Because of the distortions, there are 4 iridium atoms in the unit cell. In the following, we therefore consider a unit cell with two Ir dimers stacked along the c -axis.

Assuming no hopping between the $j_{\text{eff}} = 1/2$ and $j_{\text{eff}} = 3/2$ orbitals, one can restrict the description to the following 4×4 matrix for the $j_{\text{eff}} = 1/2$ bands:

$$H_0(\mathbf{k}) = \begin{pmatrix} \mathcal{O}_1(\mathbf{k}) & \mathcal{T}(\mathbf{k}) \\ \mathcal{T}(\mathbf{k})^\dagger & \mathcal{O}_2(\mathbf{k}) \end{pmatrix}. \quad (\text{A.1})$$

Here, \mathbf{k} is expressed in terms of the reciprocal vectors forming the reduced Brillouin zone. The submatrix $\mathcal{T}(\mathbf{k})$ describes the inter-layer hopping part of the Hamiltonian:

$$\mathcal{T}(\mathbf{k}) = -t_3 \begin{pmatrix} \gamma_{k_y} + e^{-ik_z} \gamma_{k_x}^* & \gamma_{k_x}^* + e^{-ik_z} \gamma_{k_y} \\ \gamma_{k_x} + e^{-ik_z} \gamma_{k_y}^* & \gamma_{k_y}^* + e^{-ik_z} \gamma_{k_x} \end{pmatrix} \quad (\text{A.2})$$

with $\gamma_{k_x} = 1 + e^{+ik_x}$ and $\gamma_{k_y} = 1 + e^{+ik_y}$. The submatrix $\mathcal{O}(\mathbf{k})$ describes the inter-layer part of the Hamiltonian, which is identical for the two layers:

$$\mathcal{O}_1(\mathbf{k}) = \mathcal{O}_2(\mathbf{k}) = \begin{pmatrix} e_{\mathbf{k}}^A & t_{\mathbf{k}} \\ t_{\mathbf{k}}^* & e_{\mathbf{k}}^B \end{pmatrix} \quad (\text{A.3})$$

where $e_{\mathbf{k}}^A = e_{\mathbf{k}}^B = \varepsilon_0 - 2t_2(\cos(k_x) + \cos(k_y)) + \varepsilon_{hyb}(\mathbf{k})$ and $t_{\mathbf{k}} = -2t_1 e^{i\frac{k_x+k_y}{2}} \gamma_1(\mathbf{k})$ with $\gamma_1(\mathbf{k}) = \cos(\frac{k_x+k_y}{2}) + \cos(\frac{k_x-k_y}{2})$. The additional term $\varepsilon_{hyb}(\mathbf{k}) = +4\varepsilon_1 \gamma_1(\mathbf{k})^2$ comes from the hybridization between the former d_{xy} and $d_{x^2-y^2}$ orbitals [96] or can also be understood as an additional in-plane next-next-nearest neighbor hopping.

The best fit was obtained with $\varepsilon_0 = -0.237$ eV, $t_1 = 0.171$ eV, $t_2 = 0.0935$ eV, $t_3 = 0.0169$ eV and $\varepsilon_1 = 0.026$ eV. Due to the inter-layer hopping t_3 , one obtains two bands: An inter-layer bonding and an inter-layer antibonding band.⁺ One can also downfold this effect and consider each layer independently. In this case, for the inter-layer bonding band, one gets the following parameters: $\varepsilon_0 = -0.217$ eV, $t_1 = 0.188$ eV, $t_2 = 0.0935$ eV and $\varepsilon_1 = 0.021$ eV, while for the antibonding band, one gets $\varepsilon_0 = -0.217$ eV, $t_1 = 0.154$ eV, $t_2 = 0.0935$ eV and $\varepsilon_1 = 0.029$ eV, see Fig. A1.

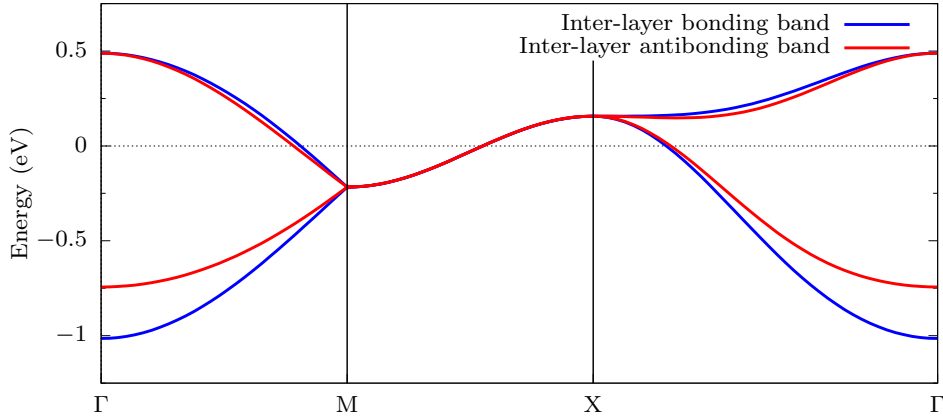


Figure A1. Tight-binding fit of the DFT bands for the two-sheet unit cell consisting of two dimers per sheet, leading to an inter-layer bonding and inter-layer antibonding band in c -direction.

Just as in DFT calculations, the filling of these tight-binding dispersions is slightly larger than half-filling. However, three-orbital DMFT calculations showed that treating the full $j_{\text{eff}}=1/2$ and $j_{\text{eff}}=3/2$ manifold leads to a charge-transfer into the $j_{\text{eff}}=3/2$ bands and results in a half-filled $j_{\text{eff}}=1/2$ band [15]. To set our one-band effective model, we take into account this charge-transfer by adjusting the chemical potential μ such that the $j_{\text{eff}}=1/2$ manifold is half-filled.

⁺ Note that the inter-layer bonding-/antibonding bands should not be confused with the bonding-/antibonding- splitting within the dimer, which we refer to in the main text.

Appendix B. Comparison of different ARPES studies on Sr_2IrO_4

In Table B1 we list the temperatures and photon energies at which the experimental ARPES measurements that were used in this article have been performed.

	Temperature T (K)	Energy $h\nu$ (eV)
<i>Kim et al.</i> 2008 [12]	100	85
<i>Wang et al.</i> 2013 [21]	25	80
<i>Liu et al.</i> 2015 [25]	20	21.2
<i>de la Torre et al.</i> 2015 [24]	50	100
<i>Brouet et al.</i> 2015 [23]	50	100
<i>Nie et al.</i> 2015 [26]	70	21.2
<i>Cao et al.</i> 2016 [28]	50	77,80,90
<i>Terashima et al.</i> 2017 [92]	100	100
<i>Martins et al.</i> 2018 [30]	300	80

Table B1. Comparison of the temperature and photon energies of the different ARPES studies on undoped Sr_2IrO_4 of which data is shown here.

References

- [1] O. Gunnarsson, E. Koch, and R. M. Martin. Mott transition in degenerate Hubbard models: Application to doped fullerenes. *Phys. Rev. B*, 54:R11026–R11029, Oct 1996.
- [2] Marcelo J. Rozenberg. Integer-filling metal-insulator transitions in the degenerate Hubbard model. *Phys. Rev. B*, 55:R4855–R4858, Feb 1997.
- [3] M. Imada, A. Fujimori, and Y. Tokura. Metal-insulator transitions. *Rev. Mod. Phys.*, 70:1039–1263, October 1998.
- [4] E. Pavarini, S. Biermann, A. Poteryaev, A. I. Lichtenstein, A. Georges, and O. K. Andersen. Mott Transition and Suppression of Orbital Fluctuations in Orthorhombic $3d^1$ Perovskites. *Phys. Rev. Lett.*, 92:176403, Apr 2004.
- [5] Jan M. Tomczak, M. Casula, T. Miyake, and S. Biermann. Asymmetry in band widening and quasiparticle lifetimes in SrVO_3 : Competition between screened exchange and local correlations from combined GW and dynamical mean-field theory $GW + \text{DMFT}$. *Phys. Rev. B*, 90:165138, Oct 2014.
- [6] P. Seth, O. E. Peil, L. Pourovskii, M. Betzinger, C. Friedrich, O. Parcollet, S. Biermann, F. Aryasetiawan, and A. Georges. Renormalization of effective interactions in a negative charge transfer insulator. *Phys. Rev. B*, 96(20):205139, November 2017.
- [7] P. A. Lee, N. Nagaosa, and X.-G. Wen. Doping a Mott insulator: Physics of high-temperature superconductivity. *Rev. Mod. Phys.*, 78:17–85, Jan 2006.
- [8] D. J. Scalapino. A common thread: The pairing interaction for unconventional superconductors. *Rev. Mod. Phys.*, 84:1383–1417, October 2012.
- [9] Henri A. What is the simplest model that captures the basic experimental facts of the physics of underdoped cuprates? *Comptes Rendus Physique*, 15(6):519 – 524, 2014.
- [10] O.K. Andersen, A.I. Lichtenstein, O. Jepsen, and F. Paulsen. LDA energy bands, low-energy hamiltonians, t' , t'' , $t_{\perp}(\mathbf{k})$, and J_{\perp} . *Journal of Physics and Chemistry of Solids*, 56(12):1573 – 1591, 1995. Proceedings of the Conference on Spectroscopies in Novel Superconductors.

- [11] W. Hanke, M.L. Kiesel, M. Aichhorn, S. Brehm, and E. Arrigoni. The 3-band Hubbard-model versus the 1-band model for the high-Tc cuprates: Pairing dynamics, superconductivity and the ground-state phase diagram. *The European Physical Journal Special Topics*, 188(1):15–32, Oct 2010.
- [12] B. J. Kim, Hosub Jin, S. J. Moon, J.-Y. Kim, B.-G. Park, C. S. Leem, Jaejun Yu, T. W. Noh, C. Kim, S.-J. Oh, J.-H. Park, V. Durairaj, G. Cao, and E. Rotenberg. Novel $J_{\text{eff}} = 1/2$ Mott State Induced by Relativistic Spin-Orbit Coupling in Sr_2IrO_4 . *Phys. Rev. Lett.*, 101:076402, Aug 2008.
- [13] C. Martins, M. Aichhorn, L. Vaugier, and S. Biermann. Reduced Effective Spin-Orbital Degeneracy and Spin-Orbital Ordering in Paramagnetic Transition-Metal Oxides: Sr_2IrO_4 versus Sr_2RhO_4 . *Phys. Rev. Lett.*, 107:266404, Dec 2011.
- [14] R. Arita, J. Kuneš, A. V. Kozhevnikov, A. G. Eguiluz, and M. Imada. Ab initio Studies on the Interplay between Spin-Orbit Interaction and Coulomb Correlation in Sr_2IrO_4 and Ba_2IrO_4 . *Phys. Rev. Lett.*, 108:086403, Feb 2012.
- [15] C. Martins, M. Aichhorn, and S. Biermann. Coulomb correlations in 4d and 5d oxides from first principles – or how spin-orbit materials choose their effective orbital degeneracies. *Journal of Physics: Condensed Matter*, 29(26):263001, 2017.
- [16] D. Haskel, G. Fabbris, Mikhail Zhernenkov, P. P. Kong, C. Q. Jin, G. Cao, and M. van Veenendaal. Pressure Tuning of the Spin-Orbit Coupled Ground State in Sr_2IrO_4 . *Phys. Rev. Lett.*, 109:027204, Jul 2012.
- [17] S. Fujiyama, H. Ohsumi, T. Komesu, J. Matsuno, B. J. Kim, M. Takata, T. Arima, and H. Takagi. Two-Dimensional Heisenberg Behavior of $J_{\text{eff}}=1/2$ Isospins in the Paramagnetic State of the Spin-Orbital Mott Insulator Sr_2IrO_4 . *Phys. Rev. Lett.*, 108:247212, Jun 2012.
- [18] J. Kim, D. Casa, M. H. Upton, T. Gog, Y.-J. Kim, J. F. Mitchell, M. van Veenendaal, M. Daghofer, J. van den Brink, G. Khaliullin, and B. J. Kim. Magnetic Excitation Spectra of Sr_2IrO_4 Probed by Resonant Inelastic X-Ray Scattering: Establishing Links to Cuprate Superconductors. *Phys. Rev. Lett.*, 108:177003, Apr 2012.
- [19] S. Fujiyama, H. Ohsumi, K. Ohashi, D. Hirai, B. J. Kim, T. Arima, M. Takata, and H. Takagi. Spin and Orbital Contributions to Magnetically Ordered Moments in 5d Layered Perovskite Sr_2IrO_4 . *Phys. Rev. Lett.*, 112:016405, Jan. 2014.
- [20] Y. K. Kim, O. Krupin, J. D. Denlinger, A. Bostwick, E. Rotenberg, Q. Zhao, J. F. Mitchell, J. W. Allen, and B. J. Kim. Fermi arcs in a doped pseudospin-1/2 Heisenberg antiferromagnet. *Science*, 345(6193):187–190, 2014.
- [21] Q. Wang, Y. Cao, J. A. Waugh, S. R. Park, T. F. Qi, O. B. Korneta, G. Cao, and D. S. Dessau. Dimensionality-controlled Mott transition and correlation effects in single-layer and bilayer perovskite iridates. *Phys. Rev. B*, 87:245109, Jun 2013.
- [22] A. Yamasaki, S. Tachibana, H. Fujiwara, A. Higashiya, A. Irizawa, O. Kirilmaz, F. Pfaff, P. Scheiderer, J. Gabel, M. Sing, T. Muro, M. Yabashi, K. Tamasaku, H. Sato, H. Namatame, M. Taniguchi, A. Hloskovskyy, H. Yoshida, H. Okabe, M. Isobe, J. Akimitsu, W. Drube, R. Claessen, T. Ishikawa, S. Imada, A. Sekiyama, and S. Suga. Bulk nature of layered perovskite iridates beyond the Mott scenario: An approach from a bulk-sensitive photoemission study. *Phys. Rev. B*, 89:121111, Mar 2014.
- [23] V. Brouet, J. Mansart, L. Perfetti, C. Piovera, I. Vobornik, P. Le Fèvre, F. Bertran, S. C. Riggs, M. C. Shapiro, P. Giraldo-Gallo, and I. R. Fisher. Transfer of spectral weight across the gap of Sr_2IrO_4 induced by La doping. *Phys. Rev. B*, 92:081117, Aug 2015.
- [24] A. de la Torre, S. McKeown Walker, F. Y. Bruno, S. Riccò, Z. Wang, I. Gutierrez Lezama, G. Scheerer, G. Girit, D. Jaccard, C. Berthod, T. K. Kim, M. Hoesch, E. C. Hunter, R. S. Perry, A. Tamai, and F. Baumberger. Collapse of the Mott Gap and Emergence of a Nodal Liquid in Lightly Doped Sr_2IrO_4 . *Phys. Rev. Lett.*, 115:176402, Oct 2015.
- [25] Y. Liu, L. Yu, X. Jia, J. Zhao, H. Weng, Y. Peng, C. Chen, Z. Xie, D. Mou, J. He, X. Liu, Y. Feng, H. Yi, L. Zhao, G. Liu, S. He, X. Dong, J. Zhang, Z. Xu, C. Chen, G. Cao, X. Dai, Z. Fang,

- and X. J. Zhou. Anomalous High-Energy Waterfall-Like Electronic Structure in 5d Transition Metal Oxide Sr_2IrO_4 with a Strong Spin-Orbit Coupling. *Sci. Rep.*, 5:13036–, August 2015.
- [26] Y. F. Nie, P. D. C. King, C. H. Kim, M. Uchida, H. I. Wei, B. D. Faeth, J. P. Ruf, J. P. C. Ruff, L. Xie, X. Pan, C. J. Fennie, D. G. Schlom, and K. M. Shen. Interplay of Spin-Orbit Interactions, Dimensionality, and Octahedral Rotations in Semimetallic SrIrO_3 . *Phys. Rev. Lett.*, 114:016401, Jan 2015.
- [27] C. Piovera, V. Brouet, E. Papalazarou, M. Caputo, M. Marsi, A. Taleb-Ibrahimi, B. J. Kim, and L. Perfetti. Time-resolved photoemission of Sr_2IrO_4 . *Phys. Rev. B*, 93:241114, Jun 2016.
- [28] Y. Cao, Q. Wang, J. A. Waugh, T. J. Reber, H. Li, X. Zhou, S. Parham, S.-R. Park, N. C. Plumb, E. Rotenberg, A. Bostwick, J. D. Denlinger, T. Qi, M. A. Hermele, G. Cao, and D. S. Dessau. Hallmarks of the Mott-metal crossover in the hole-doped pseudospin-1/2 Mott insulator Sr_2IrO_4 . *Nature Communications*, 7:11367–, March 2016.
- [29] Y. K. Kim, N. H. Sung, J. D. Denlinger, and B. J. Kim. Observation of a d-wave gap in electron-doped Sr_2IrO_4 . *Nat Phys*, 12(1):37–41, January 2016.
- [30] C. Martins, B. Lenz, L. Perfetti, V. Brouet, F. Bertran, and S. Biermann. Nonlocal Coulomb correlations in pure and electron-doped Sr_2IrO_4 : Spectral functions, Fermi surface, and pseudogap-like spectral weight distributions from oriented cluster dynamical mean-field theory. *Phys. Rev. Materials*, 2:032001, Mar 2018.
- [31] Q. Li, G. Cao, S. Okamoto, J. Yi, W. Lin, B. C. Sales, J. Yan, R. Arita, J. Kunes, A. V. Kozhevnikov, A. G. Eguiluz, M. Imada, Z. Gai, M. Pan, and D. G. Mandrus. Atomically resolved spectroscopic study of Sr_2IrO_4 : Experiment and theory. *Scientific Reports*, 3:3073, Oct 2013.
- [32] J. Dai, E. Calleja, G. Cao, and K. McElroy. Local density of states study of a spin-orbit-coupling induced Mott insulator Sr_2IrO_4 . *Phys. Rev. B*, 90:041102, Jul 2014.
- [33] S. J. Moon, H. Jin, K. W. Kim, W. S. Choi, Y. S. Lee, J. Yu, G. Cao, A. Sumi, H. Funakubo, C. Bernhard, and T. W. Noh. Dimensionality-Controlled Insulator-Metal Transition and Correlated Metallic State in 5d Transition Metal Oxides $\text{Sr}_{n+1}\text{Ir}_n\text{O}_{3n+1}$ ($n = 1, 2, \text{ and } \infty$). *Phys. Rev. Lett.*, 101:226402, Nov 2008.
- [34] S. J. Moon, H. Jin, W. S. Choi, J. S. Lee, S. S. A. Seo, J. Yu, G. Cao, T. W. Noh, and Y. S. Lee. Temperature dependence of the electronic structure of the $J_{eff} = \frac{1}{2}$ Mott insulator Sr_2IrO_4 studied by optical spectroscopy. *Phys. Rev. B*, 80:195110, Nov 2009.
- [35] D. Hsieh, F. Mahmood, D. H. Torchinsky, G. Cao, and N. Gedik. Observation of a metal-to-insulator transition with both Mott-Hubbard and Slater characteristics in Sr_2IrO_4 from time-resolved photocarrier dynamics. *Phys. Rev. B*, 86:035128, Jul 2012.
- [36] L. Zhao, D. H. Torchinsky, H. Chu, V. Ivanov, R. Lifshitz, R. Flint, T. Qi, G. Cao, and D. Hsieh. Evidence of an odd-parity hidden order in a spin-orbit coupled correlated iridate. *Nat Phys*, 12(1):32–36, January 2016.
- [37] D. Pröpper, A. N. Yaresko, M. Höppner, Y. Matiks, Y.-L. Mathis, T. Takayama, A. Matsumoto, H. Takagi, B. Keimer, and A. V. Boris. Optical anisotropy of the $J_{eff} = 1/2$ Mott insulator Sr_2IrO_4 . *Phys. Rev. B*, 94:035158, Jul 2016.
- [38] Y. Li, R. D. Schaller, M. Zhu, D. A. Walko, J. Kim, X. Ke, L. Miao, and Z. Q. Mao. Strong lattice correlation of non-equilibrium quasiparticles in a pseudospin-1/2 Mott insulator Sr_2IrO_4 . *Scientific Reports*, 6:19302, Jan 2016.
- [39] S. Chikara, O. Korneta, W. P. Crummett, L. E. DeLong, P. Schlottmann, and G. Cao. Giant magnetoelectric effect in the $J_{eff} = \frac{1}{2}$ Mott insulator Sr_2IrO_4 . *Phys. Rev. B*, 80:140407, Oct 2009.
- [40] M. Ge, T. F. Qi, O. B. Korneta, D. E. De Long, P. Schlottmann, W. P. Crummett, and G. Cao. Lattice-driven magnetoresistivity and metal-insulator transition in single-layered iridates. *Phys. Rev. B*, 84:100402, Sep 2011.
- [41] I. Pallechi, M. T. Buscaglia, V. Buscaglia, E. Gilioli, G. Lamura, F. Telesio, M.R. Cimberle, and D. Marré. Thermoelectric behavior of Ruddlesden-Popper series iridates. *Journal of Physics:*

- Condensed Matter, 28(6):065601, 2016.
- [42] Y. Klein and I. Terasaki. Insight on the electronic state of Sr_2IrO_4 revealed by cationic substitutions. Journal of Physics: Condensed Matter, 20(29):295201, 2008.
- [43] B. J. Kim, H. Ohsumi, T. Komesu, S. Sakai, T. Morita, H. Takagi, and T. Arima. Phase-Sensitive Observation of a Spin-Orbital Mott State in Sr_2IrO_4 . Science, 323(5919):1329–1332, 2009.
- [44] Guotai Z., Xiaomin G., Xingming Y., Xiaoyang G., Kang W., Jin P., Fengming Z., and X. S. Wu. Structure, magnetism, and transport properties for Ca doping in Sr_2IrO_4 . AIP Advances, 7(5):055823, 2017.
- [45] D A Zocco, J J Hamlin, B D White, B J Kim, J R Jeffries, S T Weir, Y K Vohra, J W Allen, and M B Maple. Persistent non-metallic behavior in Sr_2IrO_4 and $\text{Sr}_3\text{Ir}_2\text{O}_7$ at high pressures. Journal of Physics: Condensed Matter, 26(25):255603, 2014.
- [46] L. Fruchter, G. Collin, D. Colson, and V. Brouet. Sr_2IrO_4 magnetic phase diagram from resistivity. The European Physical Journal B, 88(6):141, Jun 2015.
- [47] H. Zhang, K. Haule, and D. Vanderbilt. Effective $J=1/2$ Insulating State in Ruddlesden-Popper Iridates: An LDA+DMFT Study. Phys. Rev. Lett., 111:246402, Dec 2013.
- [48] A. Hampel, C. Piefke, and F. Lechermann. Low-energy model and electron-hole doping asymmetry of single-layer Ruddlesden-Popper iridates. Phys. Rev. B, 92:085141, Aug 2015.
- [49] A. Moutenet, A. Georges, and M. Ferrero. Pseudogap and electronic structure of electron-doped Sr_2IrO_4 . Phys. Rev. B, 97:155109, Apr 2018.
- [50] E. M. Pärshcke, K. Wohlfeld, K. Foyevtsova, and J. van den Brink. Correlation induced electron-hole asymmetry in quasi- two-dimensional iridates. Nature Communications, 8(1):686–, 2017.
- [51] S. Zhou, K. Jiang, H. Chen, and Z. Wang. Correlation Effects and Hidden Spin-Orbit Entangled Electronic Order in Parent and Electron-Doped Iridates Sr_2IrO_4 . Phys. Rev. X, 7:041018, Oct 2017.
- [52] F. Wang and T. Senthil. Twisted Hubbard Model for Sr_2IrO_4 : Magnetism and Possible High Temperature Superconductivity. Phys. Rev. Lett., 106:136402, Mar 2011.
- [53] H. Gretarsson, N. H. Sung, J. Porras, J. Bertinshaw, C. Dietl, Jan A. N. Bruin, A. F. Bangura, Y. K. Kim, R. Dinnebier, Jungho Kim, A. Al-Zein, M. Moretti Sala, M. Krisch, M. Le Tacon, B. Keimer, and B. J. Kim. Persistent Paramagnons Deep in the Metallic Phase of $\text{Sr}_{2-x}\text{La}_x\text{IrO}_4$. Phys. Rev. Lett., 117:107001, Sep 2016.
- [54] D. Pincini, J. G. Vale, C. Donnerer, A. de la Torre, E. C. Hunter, R. Perry, M. Moretti Sala, F. Baumberger, and D. F. McMorrow. Anisotropic exchange and spin-wave damping in pure and electron-doped Sr_2IrO_4 . Phys. Rev. B, 96:075162, Aug 2017.
- [55] N. S. Headings, S. M. Hayden, R. Coldea, and T. G. Perring. Anomalous High-Energy Spin Excitations in the High- T_c Superconductor-Parent Antiferromagnet La_2CuO_4 . Phys. Rev. Lett., 105:247001, Dec 2010.
- [56] F. Ye, S. Chi, B. C. Chakoumakos, J. A. Fernandez-Baca, T. Qi, and G. Cao. Magnetic and crystal structures of Sr_2IrO_4 : A neutron diffraction study. Phys. Rev. B, 87:140406, Apr 2013.
- [57] C. Cosio-Castaneda, G. Tavizon, A. Baeza, P. de la Mora, and R. Escudero. Structure and magnetic properties of the weak ferromagnet $\text{Sr}_{2-x}\text{La}_x\text{IrO}_4$. Journal of Physics: Condensed Matter, 19(44):446210, 2007.
- [58] A. J. Gatimu, R. Berthelot, S. Muir, A. W. Sleight, and M. A. Subramanian. Synthesis and characterization of $\text{Sr}_2\text{Ir}_{1-x}\text{M}_x\text{O}_4$ ($M = \text{Ti}, \text{Fe}, \text{Co}$) solid solutions. Journal of Solid State Chemistry, 190:257 – 263, 2012.
- [59] O. B. Korneta, T. Qi, S. Chikara, S. Parkin, L. E. De Long, P. Schlottmann, and G. Cao. Electron-doped $\text{Sr}_2\text{IrO}_{4-\delta}$ ($0 \leq \delta \leq 0.04$): Evolution of a disordered $J_{\text{eff}} = \frac{1}{2}$ Mott insulator into an exotic metallic state. Phys. Rev. B, 82:115117, Sep 2010.
- [60] H. Alloul, T. Ohno, and P. Mendels. ^{89}Y NMR Evidence for a Fermi-Liquid Behavior in $\text{YBa}_2\text{Cu}_3\text{O}_{6+x}$. Phys. Rev. Lett., 63:1700–1703, Oct 1989.
- [61] L. Taillefer. Scattering and Pairing in Cuprate Superconductors. Annual Review of Condensed Matter Physics, 1(1):51–70, 2010.

- [62] A. Sacuto, Y. Gallais, M. Cazayous, M.-A. Méasson, G. D. Gu, and D. Colson. New insights into the phase diagram of the copper oxide superconductors from electronic Raman scattering. *Reports on Progress in Physics*, 76(2):022502, 2013.
- [63] A. A. Kordyuk. Pseudogap from ARPES experiment: Three gaps in cuprates and topological superconductivity (Review Article). *Low Temperature Physics*, 41(5):319–341, 2015.
- [64] C. Proust and L. Taillefer. The remarkable underlying ground states of cuprate superconductors. *ArXiv e-prints*, July 2018.
- [65] J. C. Phillips, A. Saxena, and A. R. Bishop. Pseudogaps, dopants, and strong disorder in cuprate high-temperature superconductors. *Reports on Progress in Physics*, 66(12):2111, 2003.
- [66] A. van Roekeghem, P. Richard, H. Ding, and S. Biermann. Spectral properties of transition metal pnictides and chalcogenides: Angle-resolved photoemission spectroscopy and dynamical mean-field theory. *Comptes Rendus Physique*, 17:140–163, 2016.
- [67] A. Georges, G. Kotliar, W. Krauth, and M. J. Rozenberg. Dynamical mean-field theory of strongly correlated fermion systems and the limit of infinite dimensions. *Rev. Mod. Phys.*, 68:13–125, January 1996.
- [68] G. Kotliar and D. Vollhardt. Strongly Correlated Materials: Insights From Dynamical Mean-Field Theory. *Physics Today*, 57(3):53–59, 2004.
- [69] V. I. Anisimov, A. I. Poteryaev, M. A. Korotin, A. O. Anokhin, and G. Kotliar. First-principles calculations of the electronic structure and spectra of strongly correlated systems: dynamical mean-field theory. *Journal of Physics: Condensed Matter*, 9(35):7359, 1997.
- [70] A. I. Lichtenstein and M. I. Katsnelson. Ab initio calculations of quasiparticle band structure in correlated systems: LDA++ approach. *Phys. Rev. B*, 57:6884–6895, Mar 1998.
- [71] S. Biermann. *Dynamical Mean Field Theory-Based Electronic Structure Calculations for Correlated Materials*, pages 303–345. Springer Berlin Heidelberg, 2014.
- [72] S. Biermann, A. Poteryaev, A. I. Lichtenstein, and A. Georges. Dynamical Singlets and Correlation-Assisted Peierls Transition in VO_2 . *Phys. Rev. Lett.*, 94:026404, Jan 2005.
- [73] G. Kotliar, S. Y. Savrasov, K. Haule, V. S. Oudovenko, O. Parcollet, and C. A. Marianetti. Electronic structure calculations with dynamical mean-field theory. *Rev. Mod. Phys.*, 78:865–951, August 2006.
- [74] J.-Z. Ma, A. van Roekeghem, P. Richard, Z.-H. Liu, H. Miao, L.-K. Zeng, N. Xu, M. Shi, C. Cao, J.-B. He, G.-F. Chen, Y.-L. Sun, G.-H. Cao, S.-C. Wang, S. Biermann, T. Qian, and H. Ding. Correlation-Induced Self-Doping in the Iron-Pnictide Superconductor $Ba_2Ti_2Fe_2As_4O$. *Phys. Rev. Lett.*, 113:266407, Dec 2014.
- [75] E. A. Nowadnick, J. P. Ruf, H. Park, P. D. C. King, D. G. Schlom, K. M. Shen, and A. J. Millis. Quantifying electronic correlation strength in a complex oxide: A combined DMFT and ARPES study of $LaNiO_3$. *Phys. Rev. B*, 92:245109, Dec 2015.
- [76] A. Hausoel, M. Karolak, E. Sasioglu, A. Lichtenstein, K. Held, A. Katanin, A. Toschi, and G. Sangiovanni. Local magnetic moments in iron and nickel at ambient and Earth’s core conditions. *Nature Communications*, 8:16062–, July 2017.
- [77] Atsushi Hariki, Andreas Hausoel, Giorgio Sangiovanni, and Jan Kuneš. DFT+DMFT study on soft moment magnetism and covalent bonding in $SrRu_2O_6$. *Phys. Rev. B*, 96:155135, Oct 2017.
- [78] Subhasish Mandal, R. E. Cohen, and K. Haule. Valence and spin fluctuations in the Mn-doped ferroelectric $BaTiO_3$. *Phys. Rev. B*, 98:075155, Aug 2018.
- [79] Cyril Martins. *Couplage Spin-Orbite et Interaction de Coulomb dans l’Iridate de Strontium Sr_2IrO_4* . PhD thesis, École Polytechnique, Palaiseau, 2010.
- [80] T. Maier, M. Jarrell, T. Pruschke, and M. H. Hettler. Quantum cluster theories. *Rev. Mod. Phys.*, 77:1027–1080, October 2005.
- [81] F. Aryasetiawan, M. Imada, A. Georges, G. Kotliar, S. Biermann, and A. I. Lichtenstein. Frequency-dependent local interactions and low-energy effective models from electronic structure calculations. *Phys. Rev. B*, 70:195104, Nov 2004.
- [82] S. Backes, H. Jiang, and et al. unpublished. 2019.

- [83] J. Hubbard. Electron correlations in narrow energy bands. Proceedings of the Royal Society of London. Series A. Mathematical and Physical Sciences, 276(1365):238–257, 1963.
- [84] Inka L. M. Loch. Theoretical methods for the electronic structure and magnetism of strongly correlated materials. PhD thesis, Uppsala University, Materials Theory, 2017.
- [85] J. M. Tomczak. Propriétés spectrales et optiques des matériaux fortement corrélés. PhD thesis, Ecole Polytechnique, Palaiseau, 2007.
- [86] S. Moser, L. Moreschini, A. Ebrahimi, B. Dalla Piazza, M. Isobe, H. Okabe, J. Akimitsu, V. V. Mazurenko, K. S. Kim, A. Bostwick, E. Rotenberg, J. Chang, H. M. Rønnow, and M. Griener. The electronic structure of the high-symmetry perovskite iridate Ba_2IrO_4 . New Journal of Physics, 16(1):013008, 2014.
- [87] Alex Louat. Études spectroscopiques des nouveaux états électroniques induits par fort couplage spin-orbite dans les iridates. PhD thesis, Université Paris-Saclay, Orsay, 2018.
- [88] A. Louat, F. Bert, F. Bertran, P. Le Fèvre, J. Rault, S. Biermann, C. Martins, B. Lenz, and V. Brouet. Orbital character and coherence energy scale defined by ARPES in Rh-doped Sr_2IrO_4 . in preparation, 2018.
- [89] C. Dhital, T. Hogan, Z. Yamani, C. de la Cruz, X. Chen, S. Khadka, Z. Ren, and S. D. Wilson. Neutron scattering study of correlated phase behavior in Sr_2IrO_4 . Phys. Rev. B, 87:144405, Apr 2013.
- [90] M. Potthoff. Self-energy-functional approach to systems of correlated electrons. The European Physical Journal B - Condensed Matter and Complex Systems, 32:429–436, 2003.
- [91] C. Dahnen, M. Aichhorn, W. Hanke, E. Arrighoni, and M. Potthoff. Variational cluster approach to spontaneous symmetry breaking: The itinerant antiferromagnet in two dimensions. Phys. Rev. B, 70:245110, 2004.
- [92] K. Terashima, M. Sunagawa, H. Fujiwara, T. Fukura, M. Fujii, K. Okada, K. Horigane, K. Kobayashi, R. Horie, J. Akimitsu, E. Golias, D. Marchenko, A. Varykhalov, N. L. Saini, T. Wakita, Y. Muraoka, and T. Yokoya. Evolution of the remnant Fermi-surface state in the lightly doped correlated spin-orbit insulator $Sr_{2-x}La_xIrO_4$. Phys. Rev. B, 96:041106, Jul 2017.
- [93] R. Wallauer, S. Sanna, E. Lahoud, P. Carretta, and A. Kanigel. Sensitivity of angle-resolved photoemission to short-range antiferromagnetic correlations. Phys. Rev. B, 91:245149, Jun 2015.
- [94] Thomas Ayrál, Silke Biermann, and Philipp Werner. Screening and nonlocal correlations in the extended Hubbard model from self-consistent combined *GW* and dynamical mean field theory. Phys. Rev. B, 87:125149, Mar 2013.
- [95] J. Jeong, Y. Sidis, A. Louat, V. Brouet, and P. Bourges. Time-reversal symmetry breaking hidden order in $Sr_2(Ir,Rh)O_4$. Nature Communications, 8:15119, April 2017.
- [96] H. Jin, H. Jeong, T. Ozaki, and J. Yu. Anisotropic exchange interactions of spin-orbit-integrated states in Sr_2IrO_4 . Phys. Rev. B, 80:075112, Aug 2009.
- [97] J.-M. Carter, V. Shankar, and H.-Y. Kee. Theory of metal-insulator transition in the family of perovskite iridium oxides. Phys. Rev. B, 88:035111, Jul 2013.